2016

B - > Kl(+)l(-) decay form factors from three-flavor lattice QCD

Jon A. Bailey

A. Bazavov

C. Bernard

C. M. Bouchard
Coll William & Mary, Dept Phys, Williamsburg, VA 23185 USA

Recommended Citation

Bailey, Jon A.; Bazavov, A.; Bernard, C.; and Bouchard, C. M., B - > Kl(+)l(-) decay form factors from three-flavor lattice QCD (2016). *Physical Review D*, 93(2).
10.1103/PhysRevD.93.025026

$B \to K l^+ l^-$ decay form factors from three-flavor lattice QCD

Jon A. Bailey,[1] A. Bazavov,[2] C. Bernard,[3] C. M. Bouchard,[4,*] C. DeTar,[5] Daping Du,[6] A. X. El-Khadra,[7] J. Foley,[5] E. D. Freeland,[8] E. Gámiz,[9] Steven Gottlieb,[10] U. M. Heller,[11] R. D. Jain,[7] J. Komijani,[3] A. S. Kronfeld,[12,13] J. Laiho,[6] L. Levkova,[5] Yuzhi Liu,[14] P. B. Mackenzie,[12] Y. Meurice,[15] E. T. Neil,[16,17] Si-Wei Qiu,[18,†] J. N. Simone,[12] R. Sugar,[19] D. Toussaint,[20] R.S. Van de Water,[12] and Ran Zhou[12,‡]

(Fermilab Lattice and MILC Collaborations)

[1]*Department of Physics and Astronomy, Seoul National University, Seoul, South Korea*

[2]*Physics Department, Brookhaven National Laboratory, Upton, NY, USA*

[3]*Department of Physics, Washington University, St. Louis, Missouri, USA*

[4]*Department of Physics, The Ohio State University, Columbus, OH, USA*

[5]*Department of Physics and Astronomy, University of Utah, Salt Lake City, Utah, USA*

[6]*Department of Physics, Syracuse University, Syracuse, New York, USA*

[7]*Department of Physics, University of Illinois, Urbana, Illinois, USA*

[8]*School of the Art Institute of Chicago, Chicago, Illinois, USA*

[9]*CAFPE and Departamento de Física Teórica y del Cosmos, Universidad de Granada, Granada, Spain*

[10]*Department of Physics, Indiana University, Bloomington, Indiana, USA*

[11]*American Physical Society, Ridge, New York, USA*

[12]*Fermi National Accelerator Laboratory, Batavia, Illinois, USA*

[13]*Institute for Advanced Study, Technische Universität München, Garching, Germany*

[14]*Department of Physics, University of Colorado, Boulder, CO, USA*

[15]*Department of Physics and Astronomy, University of Iowa, Iowa City, IA, USA*

[16]*Department of Physics, University of Colorado, Boulder, CO 80309, USA*

[17]*RIKEN-BNL Research Center, Brookhaven National Laboratory, Upton, NY 11973, USA*

[18]*Department of Physics and Astronomy, University of Utah, Salt Lake City, Utah, USA*

[19] *Department of Physics, University of California, Santa Barbara, California, USA*
[20] *Department of Physics, University of Arizona, Tucson, Arizona, USA*

Abstract

We compute the form factors for the $B \to Kl^+l^-$ semileptonic decay process in lattice QCD using gauge-field ensembles with 2+1 flavors of sea quark, generated by the MILC Collaboration. The ensembles span lattice spacings from 0.12 to 0.045 fm and have multiple sea-quark masses to help control the chiral extrapolation. The asqtad improved staggered action is used for the light valence and sea quarks, and the clover action with the Fermilab interpretation is used for the heavy b quark. We present results for the form factors $f_+(q^2)$, $f_0(q^2)$, and $f_T(q^2)$, where q^2 is the momentum transfer, together with a comprehensive examination of systematic errors. Lattice QCD determines the form factors for a limited range of q^2, and we use the model-independent z expansion to cover the whole kinematically allowed range. We present our final form-factor results as coefficients of the z expansion and the correlations between them, where the errors on the coefficients include statistical and all systematic uncertainties. We use this complete description of the form factors to test QCD predictions of the form factors at high and low q^2. We also compare a Standard-Model calculation of the branching ratio for $B \to Kl^+l^-$ with experimental data.

* Present address: Physics Department, College of William and Mary, Williamsburg, VA, USA
† Present address: Laboratory of Biological Modeling, NIDDK, NIH, Bethesda, Maryland, USA
‡ zhouran@fnal.gov

I. INTRODUCTION

Flavor-changing neutral-current interactions (FCNC) place important constraints on physics beyond the Standard Model. In the Standard Model, tree-level FCNC contributions vanish by the Glashow-Iliopolous-Maiani (GIM) mechanism. Even at the one-loop level, the GIM mechanism suppresses these amplitudes, as do factors of the Cabibbo-Kobayashi-Maskawa (CKM) mixing matrix. Thus, new-physics effects may be substantially larger than the small Standard-Model contribution and, hence, observable. In this paper, we present an unquenched lattice-QCD calculation of the amplitudes for the FCNC process $B \to K l^+ l^-$. Within the Standard Model and beyond, three form factors can arise, and we present results for all three. This work is part of a larger program by the Fermilab Lattice and MILC Collaborations (Fermilab/MILC) to calculate form factors for exclusive semileptonic B decays needed to test the Standard Model and search for new physics, all of which use the same lattice actions and parameters. It builds upon our previous work on charged-current semileptonic B decays, $B \to \pi l \nu$ [1, 2] and $B \to D^{(*)} l \nu$ [3–5], which are used to determine the CKM matrix elements $|V_{ub}|$ and $|V_{cb}|$ [6]. It is also part of a suite of form factors needed for searching for new physics in rare semileptonic B-decay processes such as $B \to \pi l^+ l^-$ [7], $B \to D \tau \nu$ [8] and $B_s \to \mu^+ \mu^-$ [9].

Experimental research on rare B-meson decays is active [10, 11]. The BaBar, Belle, and CDF Collaborations have measured the differential branching ratio, the forward-backward asymmetry and other observables for both $B \to K l^+ l^-$ and $B \to K^* l^+ l^-$ decays [12–16]. The LHCb Collaboration has reported more precise results for the $B^0 \to K^0 l^+ l^-$ and $B^\pm \to K^\pm l^+ l^-$ decays [17–19]. The high-intensity B factories will also have results in the future [20]. Thus, it is timely to improve the precision of the theoretical calculation of these processes. Recently, the HPQCD Collaboration published the first three-flavor lattice calculation of $B \to K l^+ l^-$ [21], also analyzing the phenomenological implications [22]. Three-flavor results for the modes with vector mesons in the final state, $B \to K^* l^+ l^-$ and $B_s \to \phi l^+ l^-$, have also been presented [23].

The theoretical description of the $B \to K^{(*)} l^+ l^-$ process is based on the operator-product expansion, which leads to a low-energy effective Hamiltonian [24–27]. Amplitudes are expressed in terms of Wilson coefficients that encode the high-scale physics and hadronic matrix elements that capture the low-energy nonperturbative QCD contributions. Hadronic

matrix elements of local operators can be parameterized in terms of form factors. The uncertainties in the form factors are an important source of error in the theoretical predictions of the observables mentioned above. In order to calculate the form factors, one requires knowledge of nonperturbative QCD dynamics, and lattice QCD is the tool of choice. We focus on $B \to K l^+ l^-$, rather than $B \to K^* l^+ l^-$, because the former is a "gold-plated" decay with a stable hadron (under strong interactions) in the final state. In the vector-meson case, the K^* is unstable, and the resonance would have to be distinguished from $K\pi$ states.

The goal of this work is to improve our knowledge of the $B \to K l^+ l^-$ form factors. We use the three-flavor gauge-field ensembles generated by the MILC Collaboration with dynamical up, down, and strange quarks. We extrapolate our lattice simulation data to the physical light-quark masses and continuum using SU(2) chiral perturbation theory formulated for the process $B \to K l^+ l^-$. Because the strange-quark mass is integrated out of the SU(2) theory, the use of SU(2) χPT, rather than SU(3), improves the convergence of the chiral expansion, thereby reducing the systematic uncertainty due to the chiral-continuum extrapolation. On currently available lattices, we directly obtain the form factors at large momentum-transfer (low recoil), $q^2 \gtrsim 17$ GeV^2. Following Ref. [1], we use the z expansion to extend the lattice-QCD calculation to the full range of q^2. Compared with the work of the HPQCD Collaboration [21, 22], we use twice as many ensembles, covering a larger range of lattice spacings and using lighter sea-quark masses. In particular, the smallest lattice spacing and the smallest light-quark mass in our ensemble set are smaller by a factor of two compared to the set used by HPQCD. In addition, we use the Sheikholeslami-Wohlert (SW) action [28] with the Fermilab interpretation [29] for the b-quark, while the HPQCD Collaboration uses a nonrelativistic QCD (NRQCD) b-quark [30]. As discussed below, details of the chiral-continuum extrapolation and the z expansion also differ.

This paper is organized as follows. In Sec. II, we define the form factors for the $B \to K l^+ l^-$ decay. We then describe the lattice ensembles used in our simulations. We also discuss the formalism for the light and heavy quarks. In Sec III, we present the numerical analysis. This section has four parts. We first present results for the simulated K and B meson masses. Next, we determine the lattice form factors from two-point and three-point correlation functions. We then correct our form-factor data to account for the slight difference between the simulated b-quark mass and the physical b-quark mass. Last, we extrapolate the lattice simulation results to the chiral and continuum limits with SU(2)

heavy meson rooted staggered chiral perturbation theory (HMrSχPT). In Sec. IV, we analyze the systematic errors in our calculation and give a complete error budget for the range of momenta $q^2 \gtrsim 17$ GeV^2 accessible in our numerical simulations. In Sec. V, we extrapolate our form factors from low to high recoil using the z expansion [31–34]. We present our final results for $f_+(q^2)$, $f_0(q^2)$, and $f_T(q^2)$, including statistical and all systematic errors, as coefficients of the z expansion and the correlations between them; this provides a complete description of our form factors valid over the entire kinematic range. In Sec. VI, we use these results to test predictions for the form factor from heavy-quark symmetry at high q^2 and from QCD factorization at low q^2. Finally, we compare our form factors with other lattice-QCD and light-cone-sum-rule results, and present an outlook for future work, in Sec. VII.

Preliminary results have been reported in Refs. [35–37]. Here we present a full analysis that includes the tensor-current form factor and complete systematic error budgets.

II. LATTICE CALCULATION

In this section, we present the methods and ingredients used in this work. We give the definitions of the form factors for the $B \to Kl^+l^-$ process and their relation to physical observables in Sec. II A. We then describe the lattice actions and parameters used for gluon and fermion fields in our simulation in Sec. II B. Finally, we define the lattice currents in Sec. II C.

A. Matrix Elements and Form Factors

An operator-product expansion analysis of the $B \to Kl^+l^-$ decay in the Standard Model shows that two currents, a vector current $\mathcal{V}^\mu = \bar{s}\gamma^\mu b$ and a tensor current $\mathcal{T}^{\mu\nu} = i\bar{s}\sigma^{\mu\nu}b$, contribute to the $b \to s$ process at lowest order [10]. In general Standard Model extensions, a scalar current $\mathcal{S} = \bar{s}b$ can also arise. The matrix elements of the vector, tensor, and scalar current are characterized by three form factors $f_+(q^2)$, $f_0(q^2)$, and $f_T(q^2)$, which are

defined via

$$\langle K|\bar{s}\gamma^\mu b|B\rangle = f_+(q^2)\left(p^\mu + k^\mu - \frac{M_B^2 - M_K^2}{q^2}q^\mu\right) + f_0(q^2)\frac{M_B^2 - M_K^2}{q^2}q^\mu, \tag{2.1}$$

$$\langle K|i\bar{s}\sigma^{\mu\nu} b|B\rangle = \frac{2f_T(q^2)}{M_B + M_K}(p^\mu k^\nu - p^\nu k^\mu), \tag{2.2}$$

$$\langle K|\bar{s}b|B\rangle = \frac{M_B^2 - M_K^2}{m_b - m_s}f_0(q^2), \tag{2.3}$$

where p and k are the B-meson and kaon momenta, respectively, and $q = p - k$ is the momentum carried off by the leptons. The Ward identity relating the matrix element of a vector current to that of the corresponding scalar current ensures that f_0 is the same in Eqs. (2.1) and (2.3).

For the analysis that follows, it is convenient to write the vector-current matrix element as

$$\langle K|\bar{s}\gamma^\mu b|B\rangle = \sqrt{2M_B}\left[v^\mu f_\parallel(E_K) + k_\perp^\mu f_\perp(E_K)\right], \tag{2.4}$$

where $v^\mu = p^\mu/M_B$ is the four-velocity of the B meson, $k_\perp^\mu = k^\mu - (k\cdot v)v^\mu$, and $E_K = v\cdot k$ is the kaon energy in the B-meson rest frame. From energy-momentum conservation, $q^2 = M_B^2 + M_K^2 - 2M_B E_K$. We obtain $f_\parallel(E_K)$ and $f_\perp(E_K)$ from the temporal and spatial components of the matrix element of the vector current:

$$f_\parallel(E_K) = \frac{\langle K|\bar{s}\gamma^0 b|B\rangle}{\sqrt{2M_B}}, \tag{2.5}$$

$$f_\perp(E_K) = \frac{\langle K|\bar{s}\gamma^i b|B\rangle}{\sqrt{2M_B}k^i}. \tag{2.6}$$

Similarly, we obtain the tensor form factor f_T from

$$f_T(q^2) = \frac{M_B + M_K}{\sqrt{2M_B}}\frac{\langle K|\bar{s}\sigma^{0i} b|B\rangle}{\sqrt{2M_B}k^i}. \tag{2.7}$$

Finally, the vector and scalar form factors f_+ and f_0 can be obtained from

$$f_+(q^2) = \frac{1}{\sqrt{2M_B}}\left[f_\parallel(E_K) + (M_B - E_K)f_\perp(E_K)\right], \tag{2.8}$$

$$f_0(q^2) = \frac{\sqrt{2M_B}}{M_B^2 - M_K^2}\left[(M_B - E_K)f_\parallel(E_K) + (E_K^2 - M_K^2)f_\perp(E_K)\right]. \tag{2.9}$$

Equations (2.8) and (2.9) satisfy the kinematic constraint, $f_+(0) = f_0(0)$, automatically. At low recoil, the form factor $f_\perp$ gives the dominant contribution to f_+.

Physical observables can be described in terms of the form factors, if we neglect non-factorizable contributions. For example, the Standard-Model differential decay rate for

$B \to K l^+ l^-$ is [24, 38, 39]

$$\frac{d\Gamma}{dq^2} = \frac{G_F^2 \alpha^2 |V_{tb} V_{ts}^*|^2}{2^7 \pi^5} |\boldsymbol{k}| \beta_+ \left\{ \frac{2}{3} |\boldsymbol{k}|^2 \beta_+^2 \left| C_{10}^{\rm eff} f_+(q^2) \right|^2 + \frac{m_l^2 (M_B^2 - M_K^2)^2}{q^2 M_B^2} \left| C_{10}^{\rm eff} f_0(q^2) \right|^2 \right.$$
$$\left. + |\boldsymbol{k}|^2 \left[1 - \frac{1}{3} \beta_+^2 \right] \left| C_9^{\rm eff} f_+(q^2) + 2 C_7^{\rm eff} \frac{m_b + m_s}{M_B + M_K} f_T(q^2) \right|^2 \right\}, \tag{2.10}$$

where G_F, α, and V_{tq} are the Fermi constant, the (QED) fine structure constant, and CKM matrix elements, respectively, $|\boldsymbol{k}| = \sqrt{E_K^2 - M_K^2}$ is the kaon momentum in the B-meson rest frame, and $\beta_+^2 = 1 - 4m_l^2/q^2$, with m_l the lepton mass. The $C_i^{\rm eff}$ are effective Wilson coefficients [25]; we follow the notation of Ref. [27] in Eq. (2.10). When q^2 corresponds to a charmonium resonance, further contributions must be added to Eq. (2.10). Beyond the Standard Model, the expression can become more complicated, but $f_+(q^2)$, $f_T(q^2)$, and $f_0(q^2)$ still suffice.

B. Actions and parameters

Our calculations employ the $N_f = 2 + 1$ flavor gauge configurations generated by the MILC Collaboration [57, 58], which include the effects of dynamical u, d, and s quarks. The one-loop improved Lüscher-Weisz action is used for the gluon fields, which leads to lattice artifacts of $\mathcal{O}(\alpha_s a^2)$ [59]. (The gluon-loop correction is included [60], but not that of the quark loop [61].)

For light quarks (u, d and s), these configurations employ the a^2 tadpole-improved staggered action (asqtad) [62–68], leading to discretization errors of $\mathcal{O}(\alpha_s a^2)$ and $\mathcal{O}(a^4)$ [40]. The sea quarks are simulated with the fourth root of the staggered fermion determinant. Several theoretical and numerical analyses support the idea that this procedure yields continuum QCD as the lattice spacing $a \to 0$ [40, 69–81].

Table I summarizes the properties of the ensembles used in this work. We use the asqtad ensembles at four lattice spacings: $a \approx 0.12$ fm, $a \approx 0.09$ fm, $a \approx 0.06$ fm, and $a \approx 0.045$ fm. The volumes of the lattices are large enough ($M_\pi L \gtrsim 4$) to suppress finite-volume effects. The strange sea-quark mass is tuned to be close to its physical value. The light-to-strange sea-quark mass ratios range from $am_l'/am_h' = 0.2$ down to 0.05, to facilitate reliable chiral extrapolations. On the $a \approx 0.12$ fm and $a \approx 0.09$ fm ensembles, we use unitary data, with the light and strange valence-quark masses set equal to the corresponding sea-quark masses,

TABLE I. Parameters of the QCD gauge-field ensembles and light valence-quark masses used in this work, lattice spacing a, lattice size $N_s^3 \times N_t$, sea-quark masses am_l' and am_h', light-valence mass am_l, daughter mass am_h, the number of configurations and sources denoted as $N_{\rm conf} \times N_{\rm src}$, and the box size times the pion mass. On all ensembles but one, we use the same light valence- and sea-quark mass. (The only exception is on the $a \approx 0.09$ fm ensemble with $m_l' = 0.0465$, where the light valence-quark mass is 0.0047 instead of 0.00465.) On the $a \approx 0.12$ fm and $a \approx 0.09$ fm ensembles we also use the same valence and sea strange-quark mass. On the $a \approx 0.06$ fm and $a \approx 0.045$ fm ensembles, we use slightly different valence strange-quark masses than in the sea; the valence masses are tuned to be closer to the physical value. The values of $M_\pi L$ are taken from Refs. [4, 40]. The gauge-field configurations can be downloaded using the digital object identifier (DOI) links provided in Refs. [41–56].

$\approx a$ (fm)	$N_s^3 \times N_t$	am_l'	am_h'	am_l	am_h	$N_{\rm conf} \times N_{\rm src}$	$M_\pi L$
0.12 [41, 42]	$20^3 \times 64$	0.01	0.05	0.01	0.05	2259×4	4.5
0.12 [43]	$20^3 \times 64$	0.007	0.05	0.007	0.05	2110×4	3.8
0.12 [44]	$24^3 \times 64$	0.005	0.05	0.005	0.05	2099×4	3.8
0.09 [45–47]	$28^3 \times 96$	0.0062	0.031	0.0062	0.031	1931×4	4.1
0.09 [48]	$32^3 \times 96$	0.00465	0.031	0.0047	0.031	984×4	4.1
0.09 [49, 50]	$40^3 \times 96$	0.0031	0.031	0.0031	0.031	1015×4	4.2
0.09 [51]	$64^3 \times 94$	0.00155	0.031	0.00155	0.031	791×4	4.8
0.06 [52, 53]	$48^3 \times 144$	0.0036	0.0180	0.0036	0.0188	673×4	4.5
0.06 [54, 55]	$64^3 \times 144$	0.0018	0.0180	0.0018	0.0188	827×4	4.3
0.045 [56]	$64^3 \times 192$	0.0028	0.0140	0.0028	0.0130	801×4	4.6

with one exception. On the $a \approx 0.06$ fm and $a \approx 0.045$ fm ensembles, however, we use valence strange-quark masses that are closer to the physical value and, thus, differ slightly from the strange-quark mass in the sea.

On each configuration, we compute the correlation functions starting at four different source locations, to increase the available statistics. We first translate the gauge field by a different random four-vector on each configuration and then fix the spatial source locations at $\boldsymbol{x} = \boldsymbol{0}$ and the temporal source locations at $t = 0$, $N_t/4$, $N_t/2$, and $3N_t/4$. The correlation between the results from different source locations is weak. The random translation of the

TABLE II. Parameters used in the simulation of the heavy b quark [4]. We list the clover coefficient $c_{\rm SW}$, input b-quark hopping parameter κ'_b, and rotation coefficient d_1.

$\approx a$ (fm)	am'_l	$c_{\rm SW}$	κ'_b	d_1
0.12	0.01	1.531	0.0901	0.093340
0.12	0.007	1.530	0.0901	0.093320
0.12	0.005	1.530	0.0901	0.093320
0.09	0.0062	1.476	0.0979	0.096765
0.09	0.00465	1.477	0.0977	0.096708
0.09	0.0031	1.478	0.0976	0.096690
0.09	0.00155	1.4784	0.0976	0.096700
0.06	0.0036	1.4287	0.1052	0.096300
0.06	0.0018	1.4298	0.1052	0.096300
0.045	0.0028	1.3943	0.1143	0.08864

gauge field reduces autocorrelations between successive configurations.

For the heavy b quark, we use the Sheikholeslami-Wohlert (SW) action [28] with the Fermilab interpretation [29]. The lattice action and currents are matched to the continuum QCD action via HQET [82]. The heavy-quark action can be systematically improved to arbitrarily high orders in $1/m_b$—or, equivalently, a—by including higher-dimensional operators in the lattice action [29, 82, 83] and currents [84–86]. In this work, we remove the leading discretization errors in the action by tuning the hopping parameter κ and clover coefficient $c_{\rm SW}$. We fix the bare b-quark mass by tuning the value of κ_b to reproduce the spin-averaged B_s meson kinetic mass as in Ref. [4]. We use the tadpole-improved tree-level value for $c_{\rm SW} = u_0^{-3}$, where u_0 is obtained from the fourth-root of the plaquette. We also remove the leading discretization error in the vector and tensor currents; see Sec. II C. The values of the parameters for b quarks used in our simulations are listed in Table II.

To extrapolate the form factors calculated on the lattice to the continuum limit, we need a unified scale to compare the results from different spacings and convert to physical units. We do so with the scale r_1 which is defined such that $r_1^2 F(r_1) = 1.0$ [87, 88]. Here $F(r)$ is the force between static quarks at distance r. We first determine the relative scale r_1/a on each ensemble, and then interpolate r_1/a with a smooth function of the gauge coupling β;

TABLE III. Relative scales r_1/a used in this work, for corresponding values of β [4, 40]. The statistical and systematic errors on r_1/a are both 0.1–0.3% [4]. We also list the Goldstone pion mass (M_π) and root-mean-square (RMS) pion mass ($M_\pi^{\rm RMS}$) here.

$\approx a$ (fm)	am'_l/am'_h	β	r_1/a	M_π(MeV)	$M_\pi^{\rm RMS}$(MeV)
0.12	0.01/0.05	6.760	2.739	389	532
0.12	0.007/0.05	6.760	2.739	327	488
0.12	0.005/0.05	6.760	2.739	277	456
0.09	0.0062/0.031	7.090	3.789	354	413
0.09	0.00465/0.031	7.085	3.772	307	374
0.09	0.0031/0.031	7.080	3.755	249	329
0.09	0.00155/0.031	7.075	3.738	177	277
0.06	0.0036/0.018	7.470	5.353	316	340
0.06	0.0018/0.018	7.460	5.307	224	255
0.045	0.0028/0.014	7.810	7.208	324	331

the smoothed r_1 values are independent of the light sea-quark mass. (The explicit form of the smoothing function is given in Ref. [4].) In this paper, we choose a mass-independent scheme for r_1/a, so that it is the same for all sea masses with the same approximate lattice spacing. We use the values of r_1/a to convert all lattice quantities to r_1 units. We can then combine results from different ensembles and perform a chiral-continuum extrapolation. The physical value $r_1 = 0.3117(22)$ fm [40, 89] is determined by requiring that the continuum limit of the pion decay constant at the physical quark masses takes the PDG value [6]. The RBC-UKQCD collaboration also reported the physical value $r_1 = 0.323(8)(4)$ fm in Ref. [90]. This result is consistent with the one we use, but less precise. The values of r_1/a used in this work are provided in Table III.

C. Definition of currents

We define the current operators on the lattice as in Refs. [1, 91]:

$$V_\xi^\mu(x) = \bar{\Psi}_\alpha(x)\gamma^\mu_{\alpha\beta}\Omega_{\beta\xi}(x)\chi(x), \tag{2.11}$$

$$T_\xi^{\mu\nu}(x) = \bar{\Psi}_\alpha(x)\sigma^{\mu\nu}_{\alpha\beta}\Omega_{\beta\xi}(x)\chi(x), \tag{2.12}$$

where the matrix $\Omega = \gamma_4^{x_4/a}\gamma_1^{x_1/a}\gamma_2^{x_2/a}\gamma_3^{x_3/a}$ and $\chi(x)$ is the 1-component staggered fermion field. The clover b-quark field is rotated to remove discretization errors of order a from the lattice current [29]:

$$\Psi = (1 + ad_1\boldsymbol{\gamma}\cdot\boldsymbol{D}_{\rm lat})\,\psi, \tag{2.13}$$

where ψ is the field in the Fermilab action (for the b quark), $\boldsymbol{D}_{\rm lat}$ is the symmetric, nearest-neighbor, covariant difference operator, and d_1 is adjusted to remove discretization errors. In practice, we set the rotation coefficient d_1 to its tadpole-improved tree-level value:

$$d_1 = \frac{1}{u_0}\left(\frac{1}{2+m_0a} - \frac{1}{2(1+m_0a)}\right)\ , \tag{2.14}$$

where m_0a is the bare lattice b-quark mass. The index ξ in Eqs. (2.11) and (2.12) corresponds to taste, and it is contracted with another taste index in the heavy-light operators coupling the B meson to the vacuum [91].

To calculate the form factors on the lattice, we have to define currents with the correct continuum limit. As in earlier work [1, 82], we define

$$\mathcal{V}^\mu \doteq Z_{V^\mu}V^\mu, \tag{2.15}$$

$$\mathcal{T}^{\mu\nu} \doteq Z_{T^{\mu\nu}}T^{\mu\nu}, \tag{2.16}$$

where $\{\mathcal{V}, \mathcal{T}\}$ and $\{V, T\}$ are the continuum and lattice current operators, respectively. We use a mostly nonperturbative renormalization procedure to obtain the Z factors [92],

$$Z_J = \rho_J\sqrt{Z_{V^4_{bb}}Z_{V^4_{ss}}}, \tag{2.17}$$

where $Z_{V^4_{bb}}$ and $Z_{V^4_{ss}}$ are computed nonperturbatively, and the remaining factor ρ_J is calculated at one-loop order in mean-field improved lattice perturbation theory [84].

The light-light renormalization factor $Z_{V^4_{ss}}$ is calculated nonperturbatively from the charge normalization condition of a $\bar{c}s$ meson:

$$Z^{-1}_{V^4_{ss}} = \int d^3x\langle D_s|V^4_{ss}(x)|D_s\rangle \tag{2.18}$$

as in Ref. [89], but with random color wall sources and higher statistics, leading to the values listed in Table IV. The result for $Z_{V^4_{ss}}$ is insensitive to the mass of the spectator quark in the correlation function, so we use a heavy charm quark to improve the statistical errors. The heavy-heavy renormalization factor $Z_{V^4_{bb}}$ is computed analogously from the charge normalization condition of the B meson using data generated for our $B \to Dl\nu$ analysis [93]. We compute $Z_{V^4_{bb}}$ on the same jackknife samples as the form factors and propagate the statistical error directly throughout the remainder of the analysis. The values of $Z_{V^4_{bb}}$ are shown in Table IV.

The remaining factor ρ_J (here, $J = V^\mu$, $T^{\mu\nu}$) is close to unity [84, 94], because most of the radiative corrections, particularly those from tadpole diagrams, cancel among the Z factors in Eq. (2.17). We expand the factor ρ_J perturbatively as

$$\rho_J = 1 + \alpha_s(q^*)\rho_J^{[1]} + \mathcal{O}(\alpha_s^2), \tag{2.19}$$

where α_s is the QCD coupling [95, 96]. Details of the one-loop perturbative calculation will be given in a separate publication [97]; the values used here are listed in Table V. In practice, we evaluate the coupling in the V-scheme [95, 98] at the scale $q^* = 2/a$ in mean-field improved lattice perturbation theory. For ρ_{V^4} we find that the one-loop corrections are less than 1%, while for ρ_{V^i} they range between $1.5 - 2.6\%$. The tensor current is scale-dependent, and we renormalize it at the scale $\mu = m_b$ (where according to the Fermilab prescription $m_2 = m_b$). We find that for ρ_T the corrections range between $3 - 6\%$.

Because ρ_J is computed separately from the correlations functions, we used it to introduce a blinding procedure (as in many B physics experiments) to reduce subjective bias. Those of us carrying out the perturbative calculation [97] multiplied ρ_J by a constant prefactor. Only after we finalized the choices made in our analysis, including tests and estimates of systematic uncertainties, was the prefactor revealed to the rest of the collaboration and removed from the results reported here.

III. ANALYSIS

In this section, we present our form factor analysis and results. In Sec. III A, we obtain the B-meson and kaon masses and energies by fitting two-point correlation functions. In Sec. III B, we extract the lattice form factors from ratios of three-point over two-point

TABLE IV. The flavor-conserving renormalization factors $Z_{V^4_{ss}}$ and $Z_{V^4_{bb}}$ used in this work. Errors shown are statistical.

$\approx a$ (fm)	am'_l	am'_h	κ'_b	$Z_{V^4_{ss}}$	$Z_{V^4_{bb}}$
0.12	0.01	0.05	0.0901	1.741(3)	0.5065(57)
0.12	0.007	0.05	0.0901	1.741(3)	0.5119(75)
0.12	0.005	0.05	0.0901	1.741(3)	0.5026(71)
0.09	0.0062	0.031	0.0979	1.777(5)	0.4482(57)
0.09	0.00465	0.031	0.0977	1.776(5)	0.4694(100)
0.09	0.0031	0.031	0.0976	1.776(5)	0.4608(94)
0.09	0.00155	0.031	0.0976	1.776(5)	0.4491(116)
0.06	0.0036	0.018	0.1052	1.808(6)	0.4196(101)
0.06	0.0018	0.018	0.1052	1.807(7)	0.4100(103)
0.045	0.0028	0.014	0.1143	1.841(6)	0.3564(65)

TABLE V. Matching factors ρ_{V^4}, ρ_{V^1}, and ρ_T calculated at one loop in tadpole-improved lattice perturbation theory. Here, ρ_T brings f_T to the $\overline{\text{MS}}$ scheme at $\mu = m_2$, and m_2 should be interpreted as the pole mass.

$\approx a$ (fm)	am'_l	am'_h	am_h	κ'_b	ρ_{V^4}	ρ_{V^1}	$\rho_T(\mu = m_2)$
0.12	0.010	0.050	0.050	0.0901	1.0071	0.9737	1.0334
0.12	0.007	0.050	0.050	0.0901	1.0071	0.9737	1.0333
0.12	0.005	0.050	0.050	0.0901	1.0072	0.9738	1.0333
0.09	0.0062	0.031	0.031	0.0979	0.9997	0.9759	1.0366
0.09	0.00465	0.031	0.031	0.0977	0.9998	0.9759	1.0364
0.09	0.0031	0.031	0.031	0.0976	0.9999	0.9758	1.0364
0.09	0.00155	0.031	0.031	0.0976	0.9999	0.9757	1.0364
0.06	0.0036	0.018	0.0188	0.1052	0.9956	0.9792	1.0432
0.06	0.0018	0.018	0.0188	0.1052	0.9956	0.9792	1.0433
0.045	0.0028	0.014	0.013	0.1143	0.9943	0.9843	1.0588

correlation functions. In Sec. III C, we slightly shift the full set of lattice form-factor data from the simulated κ_b' to the physical value. In Sec. III D, we carry out the chiral-continuum extrapolation by fitting the form factors to the expression derived in heavy meson rooted staggered chiral perturbation theory (HMrSχPT).

A. B and K meson masses

We extract meson masses and energies from two-point correlation functions defined at Euclidean time t:

$$C_2(t;\boldsymbol{k}) = \sum_{\boldsymbol{x}} \langle \mathcal{O}_P(\boldsymbol{x},t)\mathcal{O}_P^\dagger(\boldsymbol{0},0)\rangle e^{-i\boldsymbol{k}\cdot\boldsymbol{x}}, \tag{3.1}$$

where the subscript P denotes the K or B pseudoscalar meson in the interpolating operator. For the kaon we use a local interpolating operator. For the B meson we use the wavefunction for bottomonium given by the Richardson potential model [99] as explained in Refs. [100–102]. We generate correlators with kaon three-momenta $\boldsymbol{k} = 2\pi(0,0,0)/L$, $2\pi(1,0,0)/L$, $2\pi(1,1,0)/L$, and $2\pi(1,1,1)/L$.

The meson masses and energies are extracted from the large-t behavior of the two-point correlation functions. By inserting a complete set of states, two-point correlation functions can be decomposed into a sum of energy levels as

$$C_2(t;\boldsymbol{k}) = \sum_m (-1)^{m(t+1)} \frac{|\langle 0|\mathcal{O}_P|P(m)\rangle|^2}{2E_P^{(m)}} e^{-E_P^{(m)}t}. \tag{3.2}$$

The amplitudes of terms with odd m oscillate in time as $(-1)^{m(t+1)}$ and are due to opposite-parity-state contributions to staggered correlators. Figure 1 shows sample kaon and B-meson scaled correlators $[C_2(t) - C_2^{(0)}(t)]/C_2^{(0)}(t)$ on the $a \approx 0.12$ fm ensemble with $m_l' = 0.1m_h'$ and momentum $\boldsymbol{k} = \boldsymbol{0}$, where

$$C_2^{(0)}(t) = \frac{|\langle 0|\mathcal{O}_P|P(0)\rangle|^2}{2E_P^{(0)}} e^{-E_P^{(0)}t} \tag{3.3}$$

is the ground-state contribution determined by our fit. The opposite-parity-state contribution is insignificant for the zero-momentum kaon but is visible for the B meson. We employ a simple strategy to fit the two-point correlators because the statistical errors in the kaon and B-meson energies contribute little to the errors in form factors, which stem primarily from the three-point correlators. For the kaon correlators, we perform two-state fits that

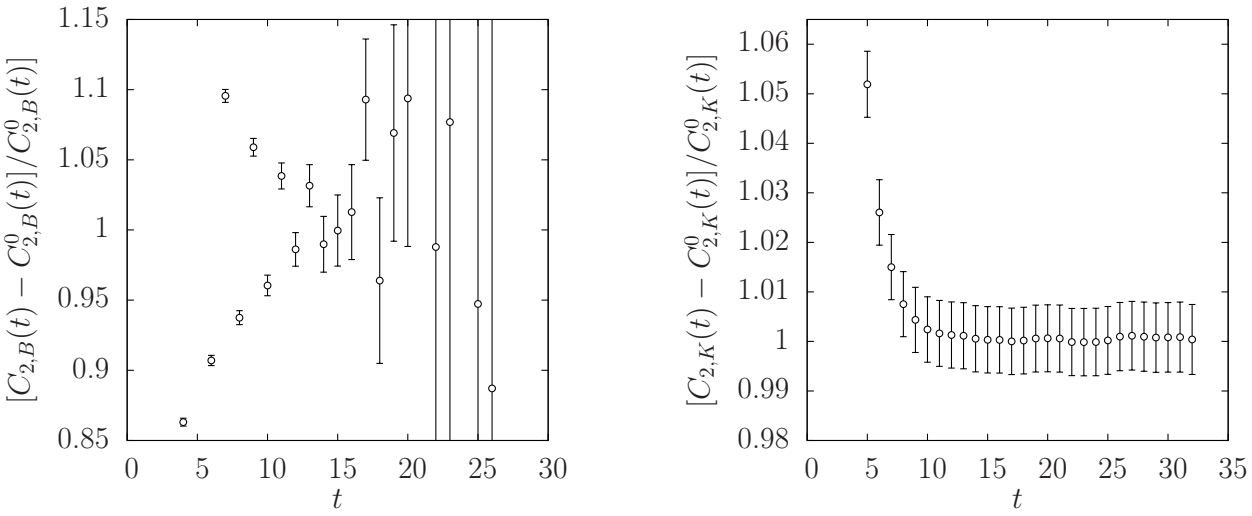

FIG. 1. Scaled correlator $[C_2(t) - C_2^{(0)}(t)]/C_2^{(0)}(t)$ as a function of time t on the $am_l'/am_h' = 0.005/0.05$ $a \approx 0.12$ fm ensemble at the unitary point. The oscillating opposite-parity-state contribution is clearly visible in the B meson correlator (left), but it is small in the zero-momentum kaon correlator (right).

include the ground state and a same-parity excited state. For the B-meson correlators, we perform three-state fits including the ground state, its excited state, and the lowest-lying opposite-parity state.

We use a single-elimination jackknife analysis to estimate the statistical errors in this work. We first average the correlation functions generated from the four sources at 0, $N_t/4$, $N_t/2$, and $3N_t/4$. We fit $C_2(t)$ in an interval $t \in [t_{\rm min}, t_{\rm max}]$, taking correlation from time slice to time slice into account. In general, we choose $t_{\rm max}$ so that the fractional error in the correlator remains below 4%. We choose $t_{\rm min}$ such that we obtain a good correlated p value. We use the same interval $[t_{\rm min}, t_{\rm max}]$ for all kaon or B-meson fits at a given lattice spacing, and use similar physical distances for $[t_{\rm min}, t_{\rm max}]$ on the four lattice spacings. These fit ranges are given in Table VI. We use a 2+1-state fit for B-meson in this paper and find consistent results with the 1+1-state, larger $t_{\rm min}$ fit of Ref. [2].

Figure 2 shows sample B-meson and kaon correlator fits versus $t_{\rm min}$ for fixed $t_{\rm max}$ on the same $a \approx 0.12$ fm ensemble as in Fig. 1. The fit results and errors are stable versus $t_{\rm min}$, and show no evidence of residual excited-state contamination.

For kaons with nonzero momentum, we can either extract the energy from two-point correlation functions with nonzero momentum, or we can use the kaon mass from the zero-

TABLE VI. Fit ranges $[t_{\rm min}, t_{\rm max}]$ used in the kaon and B-meson mass and energy fits.

$\approx a$ (fm)	kaon	B-meson
0.12	[7,30]	[3,15]
0.09	[10,35]	[5,20]
0.06	[17,60]	[7,30]
0.045	[20,90]	[8,40]

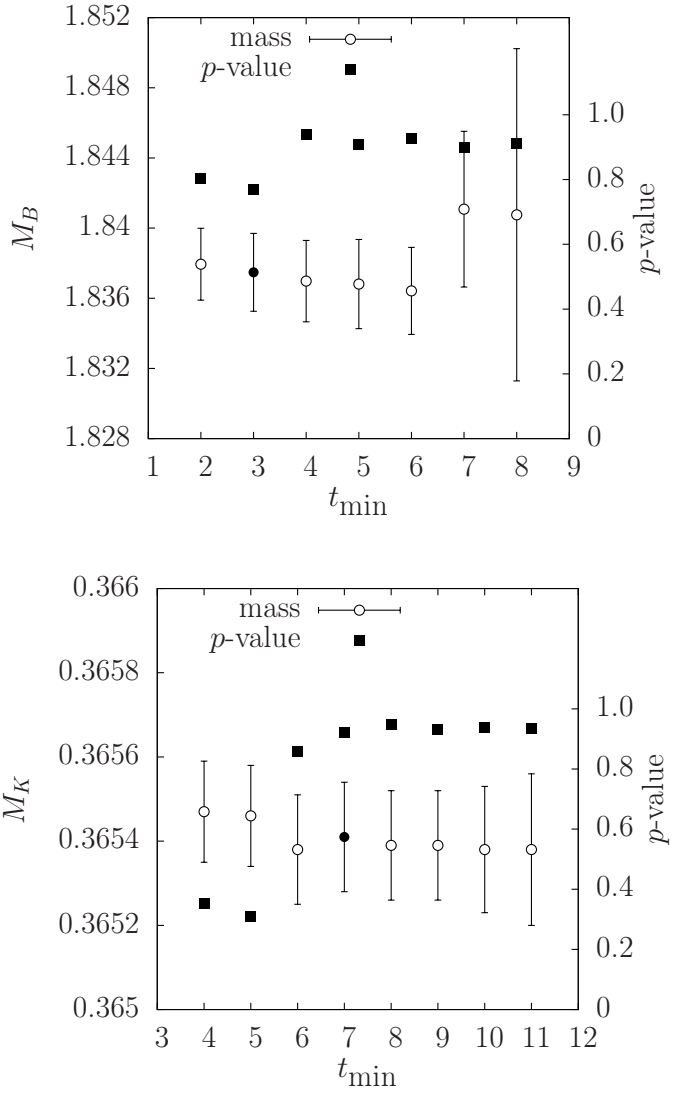

FIG. 2. B-meson (upper) and kaon (lower) mass *vs.* $t_{\rm min}$ on the $a \approx 0.12$ fm , $m'_l = 0.1 m'_h$ ensemble for fixed $t_{\rm max} = 15$ and 30, respectively. The left and right vertical-axes show the fitted mass and the p value (confidence level) of the fit, respectively. The filled circles show the values of $t_{\rm min}$ selected for the analysis.

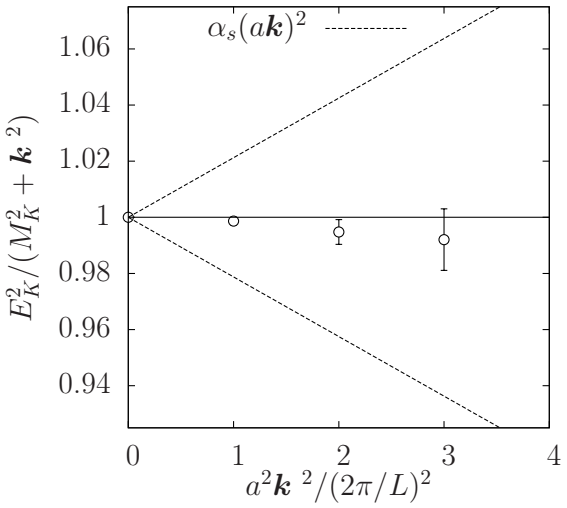

FIG. 3. $E_K^2/(M_K^2 + \boldsymbol{k}^2)$ *vs.* kaon momentum in units of $2\pi/L$ on the $a \approx 0.12$ fm , $m_l' = 0.1m_h'$ ensemble. The continuum dispersion relation is well respected through momentum $2\pi(1,1,1)/L$. The dashed lines show a power-counting estimate for the size of momentum-dependent discretization error for comparison.

momentum correlator and the continuum dispersion relation, $E^2 = M^2 + \boldsymbol{k}^2$. Figure 3 shows a comparison of the kaon energy calculated from the continuum dispersion relation and from directly fitting the nonzero momentum two-point correlation functions on the ensemble discussed above. We do not observe any statistically-significant deviations from the continuum dispersion relation. Further, while the statistical errors grow with increasing momentum, the kaon energies are consistent with a continuum dispersion relation within a 2% statistical accuracy even at our largest simulated lattice kaon momentum. Therefore, we use the continuum dispersion relation to obtain the kaon energies at nonzero lattice momenta because this yields smaller statistical errors than the direct fit.

The meson propagators from consecutive gauge-field configurations are, in principle, correlated, so we look for possible autocorrelations by studying the effect of the block size on our fit results. We perform this test on every ensemble. As illustrated in Figure 4 for two of the ensembles, the central values and errors are stable with increasing the block size, so we do not block the data or inflate the statistical errors in our analysis.

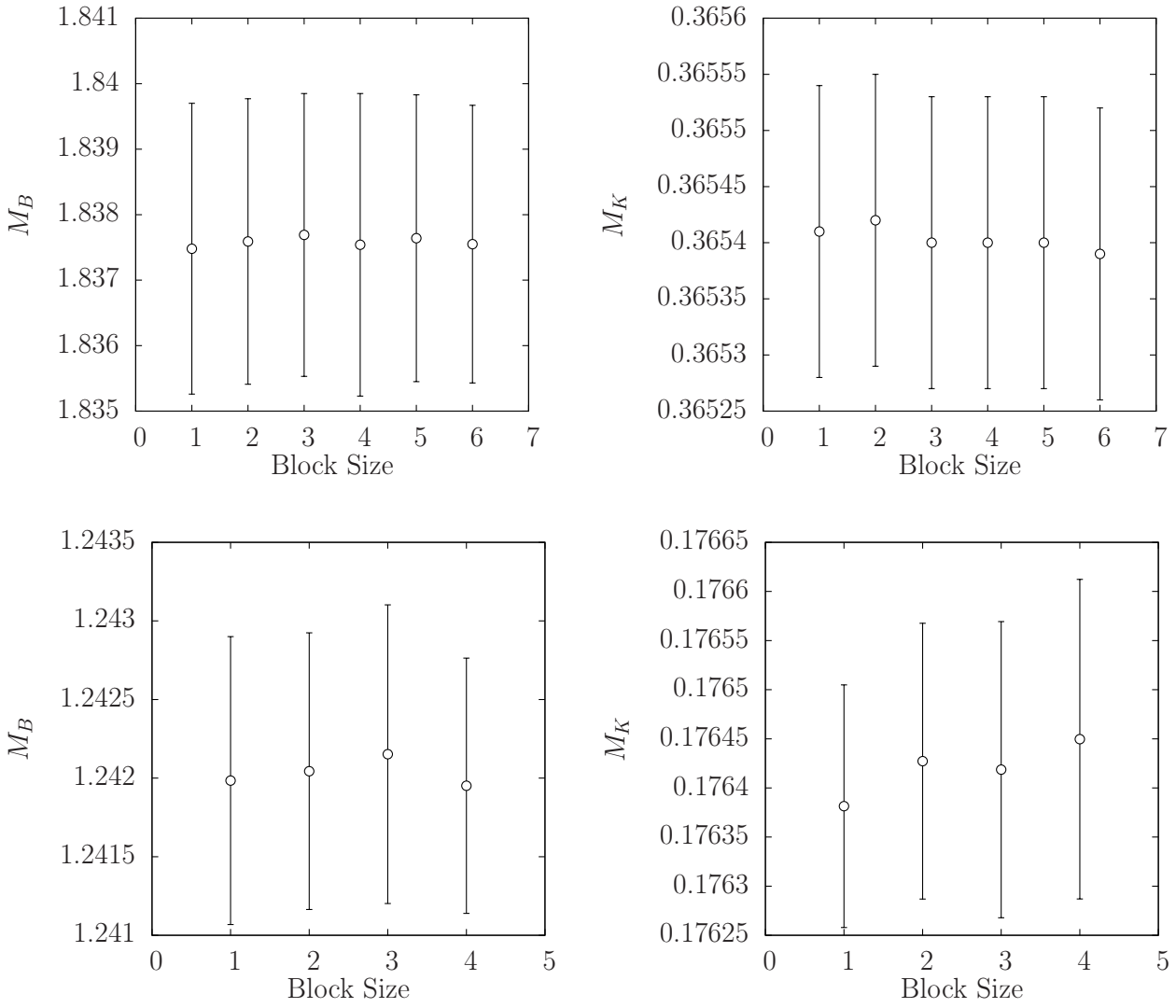

FIG. 4. M_B (left column) and M_K (right column) *vs.* block size on the $a \approx 0.12$ fm (top row) and $a \approx 0.06$ fm (bottom row), $m_l' = 0.1 m_h'$ ensemble. The fit results are stable as the block size increases.

B. Extracting form factors

We extract the lattice form factors $f_\parallel$, $f_\perp$, and f_T from the ratio of three-point to two-point correlation functions. The three-point functions are defined as

$$C_3^{\mu}(t, T; \boldsymbol{k}) = \sum_{\boldsymbol{x},\boldsymbol{y}} e^{i\boldsymbol{k}\cdot\boldsymbol{y}} \langle \mathcal{O}_K(0, \boldsymbol{0})\, V^{\mu}(t, \boldsymbol{y})\, \mathcal{O}_B^{\dagger}(T, \boldsymbol{x}) \rangle, \tag{3.4}$$

$$C_3^{\mu\nu}(t, T; \boldsymbol{k}) = \sum_{\boldsymbol{x},\boldsymbol{y}} e^{i\boldsymbol{k}\cdot\boldsymbol{y}} \langle \mathcal{O}_K(0, \boldsymbol{0})\, T^{\mu\nu}(t, \boldsymbol{y})\, \mathcal{O}_B^{\dagger}(T, \boldsymbol{x}) \rangle, \tag{3.5}$$

where the kaon source is at time slice 0 and the B-meson sink is at time slice T. The source-sink separations T are given in Table VII. Because we calculate the form factors in the B-meson rest frame, only the kaon has nonzero momentum $\boldsymbol{k}$.

By inserting two complete sets of states, the three-point correlation function C_3^μ can be decomposed into sums over energy levels as

$$C_3^\mu(t,T;\boldsymbol{k}) = \sum_{m,n}(-1)^{m(t+1)}(-1)^{n(T-t-1)}A_{mn}^\mu e^{-E_K^{(m)}t}e^{-M_B^{(n)}(T-t)}, \tag{3.6}$$

where

$$A_{mn}^\mu = \frac{\langle 0|\mathcal{O}_K|K^{(m)}\rangle}{2E_K^{(m)}}\langle K^{(m)}|V^\mu|B^{(n)}\rangle\frac{\langle B^{(n)}|\mathcal{O}_B|0\rangle}{2M_B^{(n)}}. \tag{3.7}$$

The contributions from the first few terms dominate C_3^μ at times sufficiently far from both the source and sink. A similar decomposition applies to $C_3^{\mu\nu}$.

We use the averages introduced in Ref. [1] to suppress the contribution from oscillating states in correlation functions. We average the value of the two-point correlator on successive time slices:

$$\begin{aligned}\bar{C}_2(t) &\equiv \frac{e^{-M_P^{(0)}t}}{4}\left[\frac{C_2(t)}{e^{-M_P^{(0)}t}} + \frac{2C_2(t+1)}{e^{-M_P^{(0)}(t+1)}} + \frac{C_2(t+2)}{e^{-M_P^{(0)}(t+2)}}\right] \\ &= \frac{Z_P^2}{2M_P^{(0)}}e^{-M_P^{(0)}t} + \mathcal{O}(\Delta M_P^2),\end{aligned} \tag{3.8}$$

where $Z_P = \langle 0|\mathcal{O}_P|P\rangle$ is the ground-state amplitude of the kaon or B meson, and ΔM_P is the energy difference between the ground and first oscillating state. For three-point functions, we also average the value of the correlator for two neighboring sink locations T and $T+1$:

$$\begin{aligned}\bar{C}_3^{\mu(\nu)}(t,T;\boldsymbol{k}) \equiv \frac{1}{8}&\left[e^{-E_K^{(0)}t}\,e^{-M_B^{(0)}(T-t)}\right]\times\left[\frac{C_3^{\mu(\nu)}(t,T;\boldsymbol{k})}{e^{-E_K^{(0)}t}e^{-M_B^{(0)}(T-t)}} + \frac{C_3^{\mu(\nu)}(t,T+1;\boldsymbol{k})}{e^{-E_K^{(0)}(t)}e^{-M_B^{(0)}(T+1-t)}}\right. \\ &+ \frac{2\,C_3^{\mu(\nu)}(t+1,T;\boldsymbol{k})}{e^{-E_K^{(0)}(t+1)}e^{-M_B^{(0)}(T-t-1)}} + \frac{2\,C_3^{\mu(\nu)}(t+1,T+1;\boldsymbol{k})}{e^{-E_K^{(0)}(t+1)}e^{-M_B^{(0)}(T-t)}} \\ &\left.+ \frac{C_3^{\mu(\nu)}(t+2,T;\boldsymbol{k})}{e^{-E_K^{(0)}(t+2)}e^{-M_B^{(0)}(T-t-2)}} + \frac{C_3^{\mu(\nu)}(t+2,T+1;\boldsymbol{k})}{e^{-E_K^{(0)}(t+2)}e^{-M_B^{(0)}(T-t-1)}}\right]\end{aligned} \tag{3.9}$$

$$\begin{aligned}&= A_{00}e^{-E_K^{(0)}t}\,e^{-M_B^{(0)}(T-t)} + (-1)^{T+1}A_{11}e^{-E_K^{(1)}t}e^{-M_B^{(1)}(T-t)}\left(\frac{\Delta M_B}{2}\right) \\ &\quad + \mathcal{O}(\Delta E_K^2,\,\Delta E_K\Delta M_B,\,\Delta M_B^2).\end{aligned} \tag{3.10}$$

We then form the ratios

$$\bar{R}^{\mu(\nu)}(t,T;\boldsymbol{k}) \equiv \frac{\bar{C}_3^{\mu(\nu)}(t,T;\boldsymbol{k})}{\sqrt{\bar{C}_2^K(t;\boldsymbol{k})\bar{C}_2^B(T-t)}}\sqrt{\frac{2E_K^{(0)}}{e^{-E_K^{(0)}t}\,e^{-M_B^{(0)}(T-t)}}}, \tag{3.11}$$

where $E_K^{(0)}$ and $M_B^{(0)}$ are obtained from fits to the Eq. (3.2) with $E_K^{(0)} = \sqrt{M_K^{(0)} + \boldsymbol{k}^2}$. From Eqs. (3.8) and (3.10), the ratio $\bar{R}^{\mu(\nu)}$ contains a t-independent term proportional to the desired matrix element, and other higher-order terms from the excited states.

We show an example of the ratio $\bar{R}^{\mu(\nu)}$ on the $a \approx 0.12$ fm , $m_l' = 0.1m_s'$ ensemble in Fig. 5. There is a short plateau region in the middle between 0 and T, with kaon excited-state contributions visible on the left and B-meson excited-state contributions visible on the right. The B-meson excited-state contributions, however, are smaller as indicated by the less dramatic falloff of the correlator on the right-hand side. We therefore choose to fit the correlator closer to the B-meson side including the contribution from a single B-meson excited state, but sufficiently far from the kaon that we can neglect kaon excited states. The fit function is given by:

$$\bar{R}^{\mu(\nu)}(t,T;\boldsymbol{k}) = D_0^{\mu(\nu)}\left[1 - D_1 e^{-\Delta M_B(T-t)}\right] \tag{3.12}$$

where $D_0^{\mu(\nu)}$, D_1, and ΔM_B are fit parameters. Although the second term in Eq. (3.12) models all excited states, we expect ΔM_B to be close to the mass difference of the first excited state.

We employ a correlated, constrained fit [103, 104] to Eq. (3.12), with priors determined as follows. For the prior on $D_0^{\mu(\nu)}$, we select a point from the middle of the plateau region and use its central value and with the error inflated by a factor of two. For D_1, we use a prior of central value zero and width one. For ΔM_B, we use the central value and width of $M_B^{(1)} - M_B^{(0)}$ obtained from the corresponding two-point correlator fit. We minimize the augmented χ^2_{aug} [104]

$$\chi^2_{\text{aug}} = \chi^2 + \sum_i \frac{(P^{(i)} - \tilde{P}^{(i)})^2}{\sigma_i^2}, \tag{3.13}$$

where $P^{(i)}$ is the ith fit parameter, and $\tilde{P}^{(i)}$ and σ_i are the prior central value and width. We measure the goodness of fit using the χ^2_{aug}/dof or p value, obtaining p from χ^2_{aug} and the number of degrees of freedom equal to the sum of the number of data points and prior constraints minus the number of fit parameters. We choose the fit interval $[t_{\text{min}}, t_{\text{max}}]$ such that we obtain a good p value, using the same fit range for all momenta on the same ensemble.

TABLE VII. Pairs of source-sink separations $T, T+1$ and fit ranges used in the $\bar{R}^{\mu(\nu)}$ fits.

$\approx a$ (fm)	$T, T+1$	$[t_{\rm min}, t_{\rm max}]$
0.12	18, 19	[8, 12]
0.09	25, 26	[10, 16]
0.06	36, 37	[16, 24]
0.045	48, 49	[20, 32]

We select approximately the same physical fit ranges on the ensembles with different lattice spacings. Figure 5 shows sample fits of the three form-factor ratios on the $a \approx 0.12$ fm , $m'_l = 0.1m'_s$ ensemble. Figure 6 shows an example of the stability of the fit result against the variations of the fit range. We choose the preferred fit range to be $[t_{\rm min}, t_{\rm max}] = [8, 12]$, where we find a good p value. The fit ranges and source-sink separations used on other ensembles are given in Table VII.

To study the effects of residual excited-state contamination, we generated three-point correlators on the $a \approx 0.12$ fm, $m'_l = 0.14m'_s$ ensemble with several source-sink separations $T = 18, 19, 20, 21$. We repeat the correlator fits with three sink-location combinations $(T, T+1)$=$(18, 19)$, $(19, 20)$, and $(20, 21)$, and the results are shown in Fig. 7 for four different momenta. We find no statistically-significant differences for all operators and momenta except for $f_\perp$ and f_T at $\boldsymbol{p} = 2\pi(1, 0, 0)/L$. These differences, however, are still sufficiently small that increasing the error on all $\boldsymbol{p} = 2\pi(1, 0, 0)/L$ points in the chiral-continuum fit does not change the physical form-factor results.

The fit parameters $C_0^{\mu(\nu)}$ are proportional to the matrix elements $\langle K^0|J|B^0\rangle$. The lattice form factors are obtained as

$$f_\parallel^{\rm lat}(E_K) = D_0^4(\boldsymbol{k}), \tag{3.14}$$

$$f_\perp^{\rm lat}(E_K) = \frac{D_0^i(\boldsymbol{k})}{k^i}, \tag{3.15}$$

$$f_T^{\rm lat}(E_K) = \frac{M_B + M_K}{\sqrt{2M_B}} \frac{D_0^{4i}(\boldsymbol{k})}{k^i}. \tag{3.16}$$

The factor $(M_B + M_K)/\sqrt{2M_B}$ in f_T in Eq. (3.16), which stems from Eq. (2.7), is evaluated with the physical meson masses to avoid introducing m_q dependence not captured in the χPT formula.

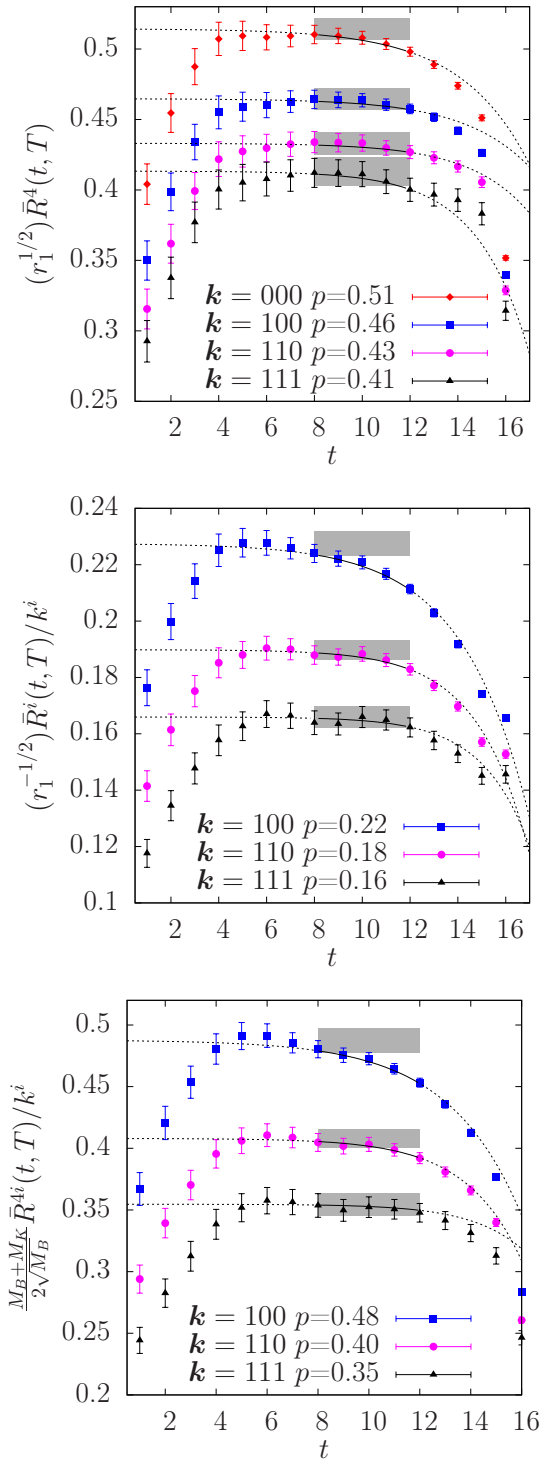

FIG. 5. Form-factor ratio $\bar{R}^{\mu(\nu)}$ fits on the $a \approx 0.12$ fm , $m_l' = 0.1 m_h'$ ensemble. From top to bottom, the three plots show the ratios for the temporal vector, spatial vector, and tensor currents. In the top plot, the data sets correspond to lattice kaon momenta $\boldsymbol{k} = 2\pi(0,0,0)/L$, $2\pi(1,0,0)/L$, $2\pi(1,1,0)/L$ and $2\pi(1,1,1)/L$; non-zero momentum is required to extract the form factors in the bottom two plots, so there are only three sets of data in each of them. The gray horizontal bands show the fit results with statistical errors for $C_0^{\mu(\nu)}$ in Eq. (3.12). The black solid and dashed curves show the fit result within and extended beyond the fit range, respectively.

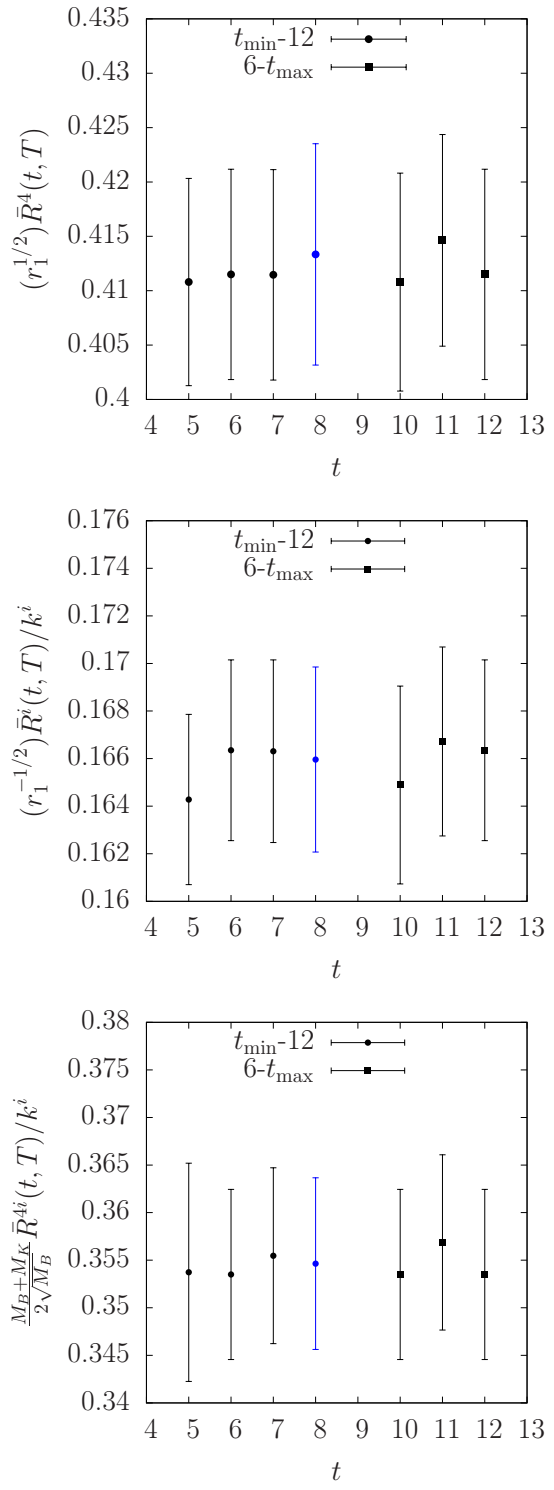

FIG. 6. Fit results of $\bar{R}^{\mu(\nu)}$ from different fit ranges on the $a \approx 0.12$ fm , $m_l' = 0.1 m_h'$ ensemble with lattice kaon momentum $p = \frac{2\pi}{L}(1,1,1)$. From top to bottom, the three plots show the ratios for the temporal vector, spatial vector, and tensor currents. We vary the fit range by changing $t_{\rm min}$ and $t_{\rm max}$. The blue data point denotes the result from the fit range used in this paper.

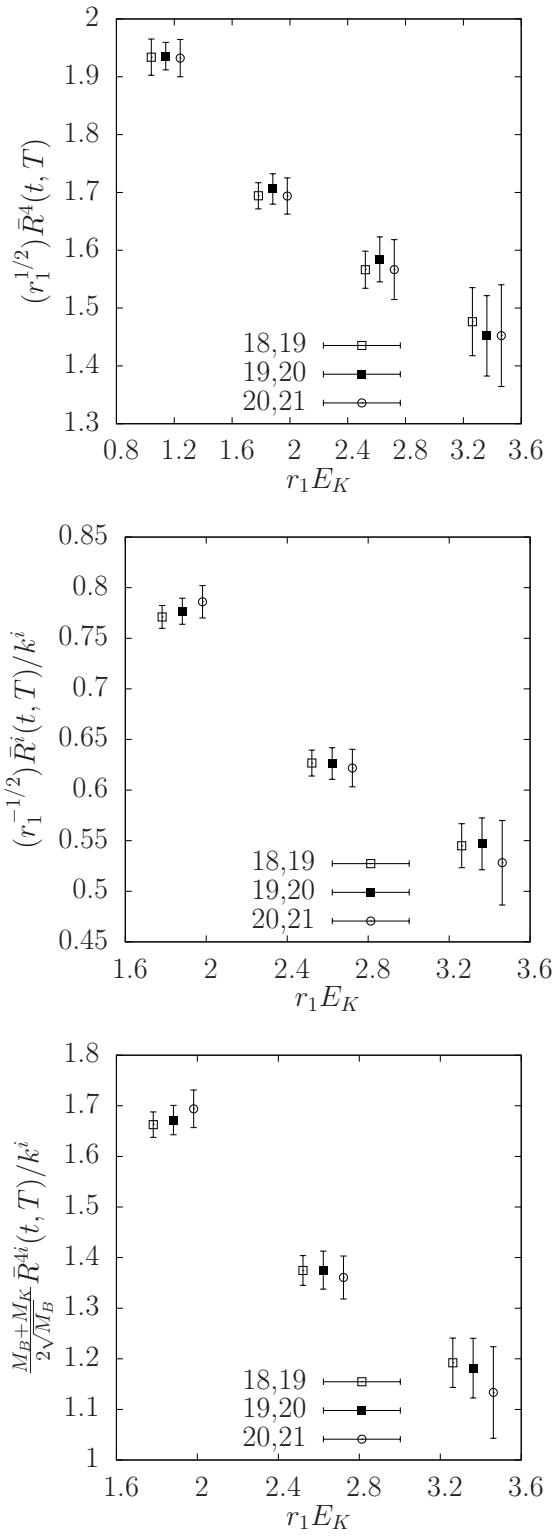

FIG. 7. Form-factor ratio $\bar{R}^{\mu(\nu)}$ fits on the $a \approx 0.12$ fm, $m'_l/m'_h = 0.007/0.05$ ensemble. From top to bottom, the three plots show the ratios for the temporal vector $f_\parallel$, spatial vector $f_\perp$, and tensor f_T currents. The fit results for different pairs of source-sink separations $T, T+1$ are shown as a function of E_K. The results from larger sink combinations are slightly displaced to the right for clarity.

C. *b*-quark mass correction

The b-quark hopping parameter used in our simulations κ_b' differs slightly from the physical value κ_b because our production runs started before a more precise tuning of the b-quark hopping parameter κ_b was completed. For our desired accuracy, we need to apply a correction. To this end, we have carried out runs with multiple values of κ_b' on the $a \approx 0.12$ fm ensemble with $m_l'/m_h' = 0.2$. In addition to the production value of $\kappa_b' = 0.0901$, we repeated the run with $\kappa_b' = 0.0820$ and 0.0860, allowing us to bracket the physical value $\kappa_b = 0.0868$. The form factors depend on the b-quark kinetic mass m_2'. At the tree level

$$\frac{1}{m_2' a} = \frac{2}{m_0' a(2 + m_0' a)} + \frac{1}{1 + m_0' a}, \tag{3.17}$$

where

$$m_0' a = \frac{1}{2u_0}\left(\frac{1}{\kappa'} - \frac{1}{\kappa_{\text{crit}}}\right). \tag{3.18}$$

The values of u_0 and κ_{crit} are given in Table VIII. Following Ref. [2], we expand the form factor in m_2^{-1} about m_2':

$$f(m_2', E_K) = f(m_2, E_K)\left[1 - \frac{\partial \ln f}{\partial \ln m_2}\left(\frac{m_2}{m_2'} - 1\right)\right] , \tag{3.19}$$

where m_2 denotes the physical b-quark kinetic mass. We determine the slope, $\frac{\partial \ln f}{\partial \ln m_2}$, in our companion work on the semileptonic decay $B \to \pi l \nu$ [2]. Because the slope depends mildly on the daughter-quark mass, and the daughter-quark mass is tuned close to its physical value in our calculation, we neglect the daughter-quark dependence of the slope in this work. Finally, we quote $\frac{\partial \ln f}{\partial \ln m_2}$ of $f_\parallel$, $f_\perp$, and f_T at the simulated daughter-quark mass as 0.115(9), 0.139(13), and 0.126(13) [2]. We find relative shifts due to b-quark mass tuning of about 0.5-1.5% on the different ensembles.

D. Chiral-continuum extrapolations

The lattice form factors are computed numerically on ensembles with degenerate up- and down-quark masses that are heavier than the value in nature, as well as at nonzero lattice spacing. To obtain physical results, we first compute the form factors on several lattice spacings with varying up/down-quark masses and close-to-physical strange-quark masses, and then extrapolate to the physical light-quark mass and continuum (and interpolate to

TABLE VIII. The simulation κ'_b and physical κ_b [4]. We also include $\kappa_{\rm crit}$ and u_0 from the plaquette in this table for convenience, because they are used in the calculation of the b-quark kinetic mass.

$\approx a$ (fm)	am'_l/am'_h	κ'_b	κ_b	$\kappa_{\rm crit}$	u_0
0.12	0.01/0.05	0.0901	0.0868(9)(3)	0.14091	0.8677
0.12	0.007/0.05	0.0901	0.0868(9)(3)	0.14095	0.8678
0.12	0.005/0.05	0.0901	0.0868(9)(3)	0.14096	0.8678
0.09	0.0062/0.031	0.0979	0.0967(7)(3)	0.139119	0.8782
0.09	0.00465/0.031	0.0977	0.0966(7)(3)	0.139134	0.8781
0.09	0.0031/0.031	0.0976	0.0965(7)(3)	0.139173	0.8779
0.09	0.00155/0.031	0.0976	0.0964(7)(3)	0.139190	0.877805
0.06	0.0036/0.018	0.1052	0.1052(5)(2)	0.137632	0.88788
0.06	0.0018/0.018	0.1052	0.1050(5)(2)	0.137678	0.88764
0.045	0.0028/0.014	0.1143	0.1116(3)(2)	0.136640	0.89511

the physical strange-quark mass) using heavy meson rooted staggered chiral perturbation theory (HMrSχPT) [105, 106].

For the chiral-continuum extrapolation we use an HMrSχPT formula valid to leading order in $1/m_b$ and next-to-leading order (NLO) in the light-quark masses, kaon energy, and lattice spacing, supplemented by next-to-next-to leading order (NNLO) analytical terms. We have tested both SU(3) HMrSχPT [106], which includes the effects of dynamical pions, kaons, and η mesons, and SU(2) HMrSχPT, in which the mesons with strange quarks are integrated out. In addition, we also consider hard-kaon HMrSχPT, which applies to semileptonic decays with energetic kaons. We find that NLO SU(3) HMrSχPT even supplemented with next-to-next-to leading order (NNLO) analytical terms, does not provide a good description of the data for $f_\parallel$ [35–37], and the p value of the fit is 10^{-9}. On the other hand, SU(2) HMrSχPT describes the data well even at NLO. We therefore choose SU(2) HMrSχPT to perform the chiral-continuum extrapolations.

The kaon energies in our numerical simulations are much larger than the rest mass of the physical kaon. Therefore standard HMrSχPT, which is derived for the situation in which the kaon momenta are soft, may not provide a good description of our data throughout the available kinematic range. We therefore also consider hard-kaon HMrSχPT, which ap-

plies for semileptonic decays with energetic kaons. Recently, Bijnens and Jemos derived the continuum NLO hard-kaon (pion) HMχPT formulae for both $B \to K$ and $B \to \pi$ processes [107, 108]. We derive the corresponding NLO staggered SU(2) and SU(3) hard kaon (pion) HMrSχPT formulae in Appendix A. It turns out that the chiral logarithms in NLO hard-kaon SU(2) HMrSχPT are identical to those in standard soft-kaon SU(2) HMrSχPT for $B \to K$ decays. This is likely the reason that the standard NLO SU(2) expressions describe our data even at such large kaon energies. Reference [109] found that the hard-pion theory can break down at three-loop level, but we only work at one-loop level here.

The NLO SU(2) HMrSχPT formulae for $B \to K$ decays take the form

$$r_1^{1/2} f_\parallel = \frac{g_\pi \left[C_\parallel^{(0)} (1 + \text{logs}) + C_\parallel^{(1)} \chi_l + C_\parallel^{(2)} \chi_h + C_\parallel^{(3)} \chi_E + C_\parallel^{(4)} \chi_{a^2} + C_\parallel^{(5)} \chi_E^2 \right]}{f_\pi r_1 (E_K + \Delta_{B_{s0}^*}) r_1}, \tag{3.20}$$

$$r_1^{-1/2} f_\perp = \frac{g_\pi \left[C_\perp^{(0)} (1 + \text{logs}) + C_\perp^{(1)} \chi_l + C_\perp^{(2)} \chi_h + C_\perp^{(3)} \chi_E + C_\perp^{(4)} \chi_{a^2} + C_\parallel^{(5)} \chi_E^2 \right]}{f_\pi r_1 (E_K + \Delta_{B_s^*}) r_1}, \tag{3.21}$$

where "logs" denotes nonanalytic functions of the light-quark mass and lattice spacing; the explicit expressions are given in Eqs. (A28), (A33), and (A34). The dimensionless expansion parameters χ_i in Eqs. (3.20) and (3.21) are

$$\chi_l = \frac{2\mu m_l}{8\pi^2 f_\pi^2}, \tag{3.22}$$

$$\chi_h = \frac{2\mu m_h}{8\pi^2 f_\pi^2}, \tag{3.23}$$

$$\chi_{a^2} = \frac{a^2 \overline{\Delta}}{8\pi^2 f_\pi^2}, \tag{3.24}$$

$$\chi_E = \frac{\sqrt{2} E_K}{4\pi f_\pi}, \tag{3.25}$$

where $a^2\overline{\Delta}$ is the averaged taste-symmetry breaking parameter, $a^2\overline{\Delta} \equiv \frac{1}{16}\sum_\xi a^2\Delta_\xi$ and μ denotes the leading-order QCD LEC; see Eqs. (A3)–(A14) for the definition. If HMrSχPT gives a good description of the data, we expect the $C^{(i)}$, $i > 0$, to be of order unity. The SU(2) χPT formulae do not contain m_h explicitly; however, the low-energy constants (LECs) depend on m_h. Because the strange-quark masses on different ensembles are slightly different from each other, we include a term proportional to χ_h in the set of analytic terms to account for the leading strange-quark mass dependence of the LECs and enable an interpolation to the physical strange-quark mass.

Equations (3.20) and (3.21) each contain a pole in E_K. The poles appear at negative energy $-\Delta_{B^*_{s(0)}}$ with

$$\Delta_{B^*_{s(0)}} \equiv \frac{M^2_{B^*_{s(0)}} - M^2_B - M^2_K}{2M_B} \approx M_{B^*_{s(0)}} - M_B. \tag{3.26}$$

The pole arises from low-lying states with flavor content $\bar{b}s$ and quantum numbers that depend upon the form factor: for $f_\perp$ and f_T, the relevant B^*_s meson has $J^P = 1^-$, while for $f_\parallel$, the B^*_{s0} state has $J^P = 0^+$. In the chiral-continuum fits, we fix M_B to its experimentally-measured value 5.27958 GeV [6] (recall that we tuned the lattice b-quark mass using the experimental B_s-meson mass.). We also use the experimentally-measured value of the lowest-lying vector meson $M_{B^*_s} = 5.4154$ GeV [6], which is stable apart from $B^*_s \to B_s\gamma$, for the pole position in the fits of $f_\perp$ and f_T to Eq. (3.21). Although a scalar B^*_{s0} state has not been observed in experiment, theoretical predictions estimate its mass to be just below the B-K production threshold [110, 111]. Therefore, in the fit of $f_\parallel$, we use the prediction $M_{B^*_{s0}} = 5.711(23)$ GeV from a recent three-flavor lattice-QCD calculation [112] for the pole position in Eq. (3.20).

Following the approach of Refs. [103, 104], we constrain the parameters of the chiral-continuum fit with Bayesian priors and minimize the augmented $\chi^2_{\rm aug}$ defined in Eq (3.13). The chiral logarithms in Eqs. (3.20) and (3.21) depend upon the universal B-B^*-π coupling g_π, which we constrain with a Gaussian prior of central value 0.45 and width 0.08. This prior is consistent with a direct lattice calculation [113–115], yet conservative enough to accommodate other lattice results [116, 117]. The chiral logarithms also depend on the mass splittings between mesons of different tastes and on the leading-order LEC μ. These parameters depend only on the light-quark action, and we fix them to the values determined in the MILC light-pseudoscalar analysis [40]; see Table IX. In the $f_\parallel$ chiral-continuum extrapolation, we account for the uncertainty on the scalar B^* mass by taking a generous prior width of three times the theoretical error reported in Ref. [112], or ± 69 MeV.

We constrain the coefficients of the LO and NLO analytic terms $C^{(0)}$–$C^{(5)}$ using priors with central values zero and widths two. To allow for higher-order contributions in the chiral expansion, we also include the complete set of NNLO analytic terms. These are proportional to χ^2_l, $\chi_l\chi_{a^2}$, $\chi_l\chi_E$, $\chi_l\chi^2_E$, $\chi_{a^2}\chi_E$, $\chi_{a^2}\chi^2_E$, χ^3_E, χ^4_E, and $\chi^2_{a^2}$. We use prior central values of 0 with widths 1 for the coefficients of the NNLO analytic terms. The systematic error from truncating the chiral expansion will be discussed in Sec.IV.

TABLE IX. Fixed parameters used in the chiral fit [4]. μ is the leading-order low-energy constant in QCD. $r_1^2 a^2 \Delta_\Xi$ and $r_1^2 a^2 \delta_{V/A}$ are the taste splittings and hairpin parameters for asqtad staggered fermions.

	$a \approx 0.12$ fm	$a \approx 0.09$ fm	$a \approx 0.06$ fm	$a \approx 0.045$ fm	continuum
$r_1\mu$	6.831904	6.638563	6.486649	6.417427	6.015349
$r_1^2 a^2 \Delta_P (10^{-2})$	0	0	0	0	0
$r_1^2 a^2 \Delta_A (10^{-2})$	22.70460	7.469220	2.634800	1.040930	0
$r_1^2 a^2 \Delta_T (10^{-2})$	36.61620	12.37760	4.297780	1.697920	0
$r_1^2 a^2 \Delta_V (10^{-2})$	48.02591	15.93220	5.743780	2.269190	0
$r_1^2 a^2 \Delta_S (10^{-2})$	60.08212	22.06520	7.038790	2.780810	0
$r_1^2 a^2 \delta_V$	0.00	0.00	0.00	0.00	0
$r_1^2 a^2 \delta_A$	-0.28	-0.09	-0.03	-0.01	0

Staggered χPT incorporates taste-breaking discretization effects from the light valence and sea quarks, but the lattice data also contain generic light-quark and gluon discretization effects as well discretization effects from the heavy quark. We account for generic light-quark and gluon discretization errors by adding the term $z\alpha_s(a\Lambda_{\rm QCD})^2$ in the HMrSχPT formulae with coefficient prior central value zero and width one. Similarly, to account for heavy-quark discretization effects in both the action and heavy-light currents, we add terms of order a^2 and $\alpha_s a$ with coefficients constrained by heavy-quark power counting [83]. At this order there are five functions (f_B, f_Y, f_3, f_E, f_X) that depend upon the bare heavy-quark mass; their explicit forms are given in Appendix A of Ref. [1]. Dimensional analysis can be used to estimate the heavy quark error

$$\texttt{error}_i \propto f_i(m_0 a)(a\Lambda)^{\dim\mathcal{O}_i - 4}, \tag{3.27}$$

where f_i is related to the mismatch between coefficients of the continuum operators in the action and currents and their lattice counterparts, and Λ is a typical QCD scale for heavy-light mesons which we take to be $\Lambda = 500$ MeV. As in Ref. [89], we add terms $z_i \times \texttt{error}_i$ to the HMrSχPT formulae for $f_{\parallel,\perp,T}$. The priors on the z_i have central values zero and widths equal to the square root of the number of times each function appears. (See Appendix A of Ref. [1].) Because the discretization errors are included via the constrained fit in the

chiral-continuum extrapolations, our results for the extrapolated form factors include the systematic uncertainties from light and heavy discretization effects.

In summary, we use expressions derived in SU(2) HMrSχPT for the central chiral-continuum extrapolations of the form factors $f_\parallel$, $f_\perp$, and f_T; these are shown in Fig. 8. The SU(2) theory describes our data well: the p values of the fits are 0.91, 0.94, and 0.98 for $f_\parallel$, $f_\perp$, and f_T, respectively. Our fit results for g_π are 0.47(5), 0.46(4), and 0.47(3), respectively. At this stage, only the statistical, g_π, chiral truncation, and discretization errors have been included. In the next section, we estimate the size of the remaining uncertainties before employing the z expansion in Sec. V to extend our results over the full kinematic range.

IV. FORM-FACTOR ERROR BUDGET

In this section, we estimate the systematic errors in the form factors, discussing each source of uncertainty in a separate subsection. We first discuss the error from the chiral-continuum extrapolation, which also includes heavy-quark, light-quark, and gluon discretization errors. We then discuss the remaining systematic uncertainties from the heavy-light current renormalization, lattice-scale determination, light- and strange-quark mass determinations, finite volume effects, and b-quark mass determination, discussing each in a separate subsection. As discussed previously, the systematic errors from g_π and heavy- and light-quark discretization effects are included in the statistical errors of the chiral-continuum extrapolation result through the constrained fit. Finally, we visually summarize the error budgets for the three form factors as a function of q^2 in Fig. 11.

A. Chiral-continuum extrapolation

We use NLO SU(2) HMrSχPT supplemented by all possible NNLO analytic terms, as well as heavy-quark, light-quark, and gluon discretization terms, in our preferred chiral extrapolations of $f_\perp$, $f_\parallel$, and f_T.

First, to estimate truncation effects, we compare fit results using NLO HMrSχPT, our preferred fit function with NNLO analytic terms, and the same fit function with the addition of the complete set of NNNLO analytic terms in Figure 9. We see that the errors in the

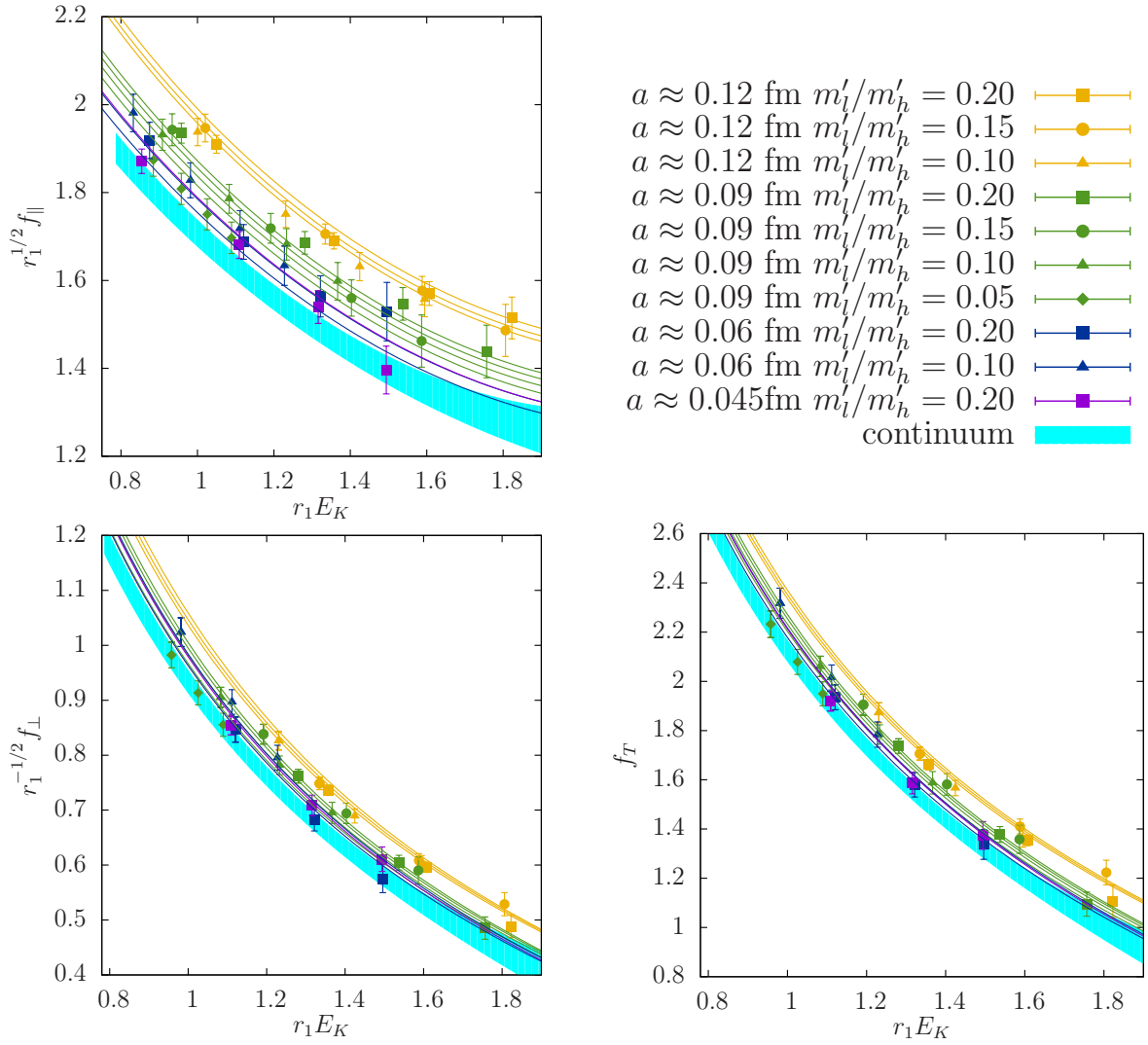

FIG. 8. Chiral-continuum extrapolations of $f_\parallel$ (upper left), $f_\perp$ (lower left), and f_T (lower right) using NLO SU(2) HMrSχPT plus NNLO analytical terms. The squares, circles, triangles, and diamonds denote the $m'_l/m'_h = 0.2$, 0.14, 0.1, and 0.05 data, respectively. The colored fit lines correspond to the different lattice spacings as indicated in the legend. The cyan band shows the continuum extrapolated curve with statistical error, which includes the systematic uncertainties due to g_π, and the heavy-quark, light-quark, and gluon discretization errors. Fit lines should pass through the data points of the corresponding color.

preferred fit with NNLO analytic terms are already saturated, since they are the same as the errors in the fit with NNNLO analytic terms. Hence, truncation effects are included in the statistical fit errors from our preferred fit.

In addition, we also consider two alternative fit Ansätze for the chiral-continuum ex-

trapolation. First, we consider NLO SU(3) hard-pion HMrSχPT, which provides a good description of our data, although the standard NLO SU(3) expressions do not. We use the result from the SU(2) HMrSχPT fit as our preferred fit, because the SU(2) theory converges faster than the SU(3) theory as studied in Ref. [118]. We compare the fit results from NLO hard-kaon SU(3) HMrSχPT plus NNLO analytical terms and our preferred fit, and find differences between the central values of about 1-2% for all form factors and q^2. Second, we consider the effect of the E_K range of the lattice-QCD data to the extrapolated continuum result by omitting the $\boldsymbol{k} = 2\pi(1,1,1)/L$ data from our fit. We find the differences are below 1-2%. Figure 10 summarizes the differences between the form factors obtained from the alternative chiral-continuum fits and the central results. Overall, the shifts of the continuum form-factors central values are within the quoted statistical errors of the preferred chiral fit that includes truncation effects.

B. Heavy-light current renormalization

To obtain the continuum form factors, we multiply the lattice form factors by the renormalization constant given in Eq. (2.17), using the values of ρ_J, $Z_{V^4_{bb}}$, and $Z_{V^4_{ss}}$ listed in Tables IV and V. The statistical error on $Z^{1/2}_{V^4_{ss}}$ is about 0.2%. By using the jackknife blocks of $Z_{V^4_{bb}}$ calculated on the same ensembles, we incorporate the statistical error from $Z^{1/2}_{V^4_{bb}}$ automatically in our fit results.

The ρ_J are calculated at one-loop order in perturbation theory. They are close to unity by design, since they are defined as ratios of renormalization factors. Indeed their one-loop corrections are small, as shown in Table V. We estimate the error due to truncating the perturbative expansion as $2\rho^{[1]}_{J,\max}\alpha_s^2$ in order to avoid sensitivity due to accidental cancellations. We obtain $\rho^{[1]}_{J,\max}$ as follows. For the scale-independent vector currents (V^i and V^4), we simply look for the largest value of the one-loop coefficients for both currents on all of the ensembles. We find that the spatial vector current has a larger one-loop coefficient with $\rho^{[1]}_{V,\max} = 0.1$. We evaluate α_s at the $a \approx 0.06$ fm lattice spacing (the next-to-finest), which yields an error of 1% for both components of the vector current. For the scale-dependent tensor current the perturbative corrections include logarithmic contributions due to its anomalous dimension, which are responsible for the growth of ρ_T towards smaller lattice spacings seen in Table V . In order to estimate the truncation error, we remove the effect

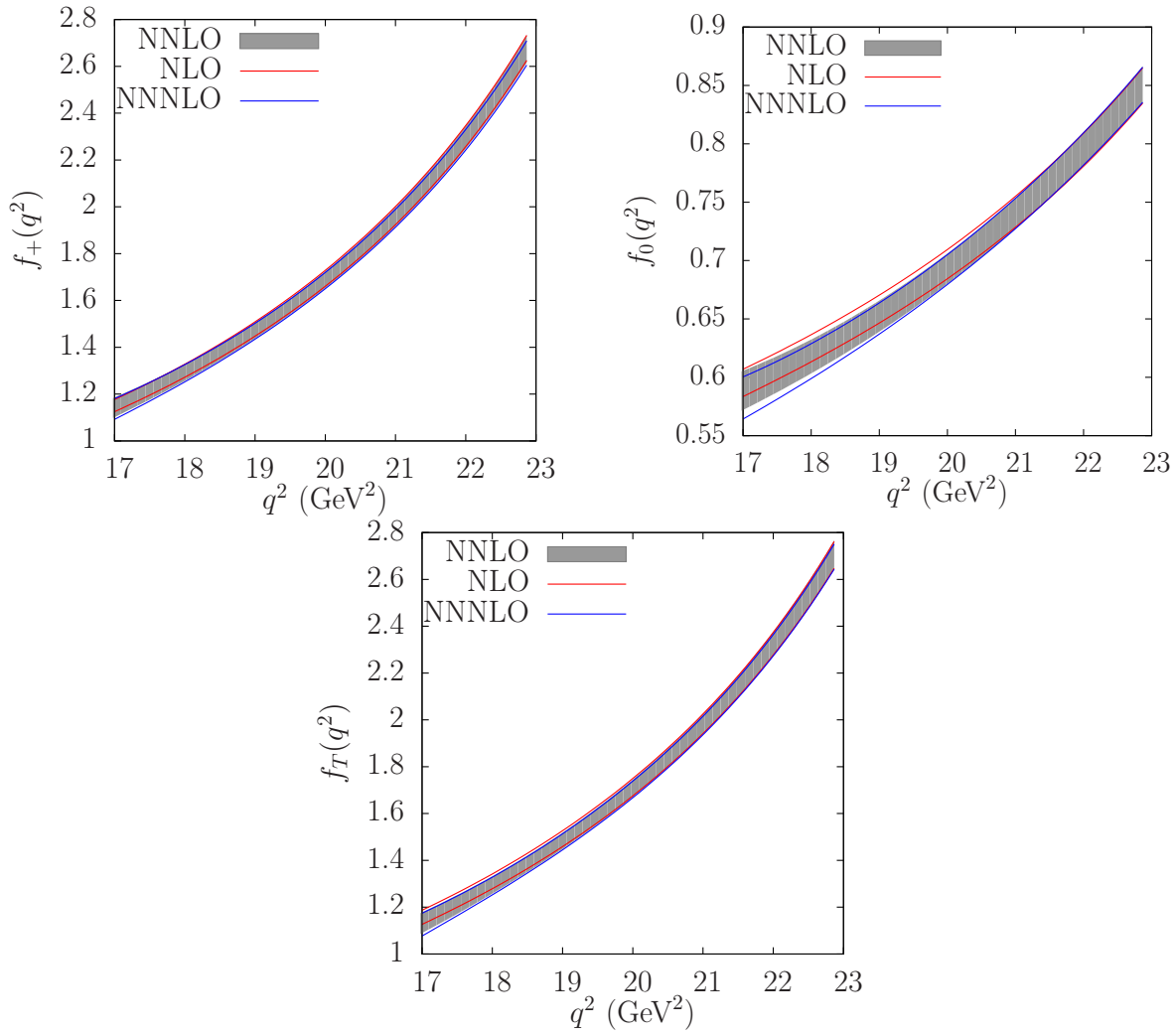

FIG. 9. Chiral-continuum extrapolations with NLO, NNLO, or NNNLO analytic terms for f_+ (upper left), f_0 (upper right), and f_T (lower panel). In each plot, the grey band shows the statistical error from the preferred NNLO SU(2) χPT. The red and blue lines show the error from the fits with NLO and NNNLO analytic terms, respectively.

of the anomalous dimension by setting $\mu = 2/a$. We find that $\rho^{[1]}_{T,\mathrm{max}} = 0.2$, which corresponds to a truncation error of 2% on ρ_T. In summary, we assign a perturbative truncation error of 1% on $f_+, 0$ and an error of 2% on f_T.

C. Scale uncertainty

We use $r_1 = 0.3117(22)$ fm in the continuum from Ref. [89] to convert lattice quantities to physical units, where the quoted error includes both statistics and systematics. We repeat

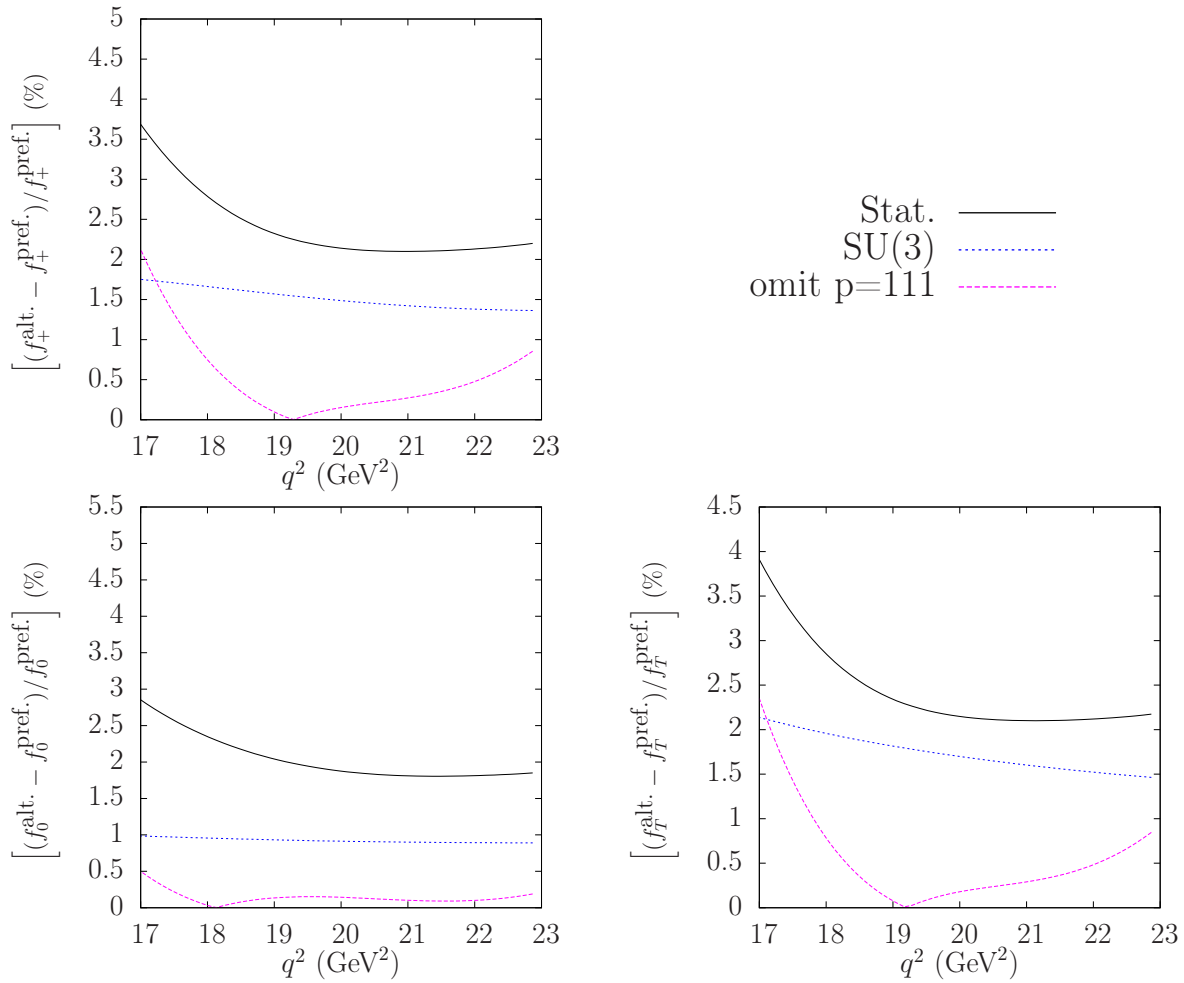

FIG. 10. Deviations of alternate chiral-continuum extrapolations from the central results for f_+ (upper left), f_0 (lower left), and f_T (lower right). In each plot, the black curve shows the statistical error from the preferred NNLO SU(2) χPT. The blue and pink lines show the % difference from the central fit obtained by using SU(3) hard-kaon χPT and omitting $\boldsymbol{k} = 2\pi(1,1,1)/L$ data, respectively.

our analysis varying r_1 by plus and minus one standard deviation from its central value and use the larger change of each form factor as an estimate of the systematic error due to the scale uncertainty. We find differences of less than 1% for $f_\parallel$, $f_\perp$, and f_T throughout the simulated q^2 region.

D. Light- and strange-quark mass uncertainties

After the chiral-continuum fit, we evaluate the form factors at the physical quark masses $r_1\hat{m} = 0.000965(33)$ and $r_1 m_s = 0.0265(8)$ determined from the analysis of the light pseudoscalar meson spectrum [4, 40]. We vary the quark masses by plus and minus one standard deviation and find the differences in all three form factors due to changing m_l and m_s to be below 0.6% in the simulated q^2 region.

E. Finite-volume effects

The lattices used in this work have finite spatial volumes with $M_\pi L \gtrsim 4$. We estimate the size of finite-volume effects using HMrSχPT. In chiral perturbation theory, finite volume contributions change loop-momentum integrals to sums which have been calculated in Refs. [106, 119]. We employ continuum integrals in the preferred chiral-continuum extrapolations. To estimate the size of finite-volume effects, we evaluate the form factors with the LECs we obtain from the preferred chiral fits, and compare the results from the infinite-volume formulae and the finite-volume formulae on all ensembles used in this work. We try both SU(2) HMrSχPT and SU(3) hard-kaon HMrSχPT. We find that in all cases finite-volume effects are below 0.001%. Therefore, we neglect finite-volume effects in the total error budget.

F. *b*-quark mass correction

We correct the form factors from the simulated κ_b' to the physical κ_b before we perform the chiral-continuum extrapolation. Including these corrections accounts for the dominant effect from b-quark mistuning, but small errors in the form factors remain due to the uncertainties in the κ_b-correction factors. The statistical errors in the slopes $\frac{\partial \ln f}{\partial \ln m_2}$ are at most about 10% for $f_{\perp,T}$ at $2\pi(1,1,1)/L$, while the sizes of the κ_b shifts applied to the data points are about 1–2%. We therefore take the the systematic error from the κ_b correction to be $2\% \times 10\% = 0.2\%$, which is conservative enough to accommodate the largest possible error in the shift.

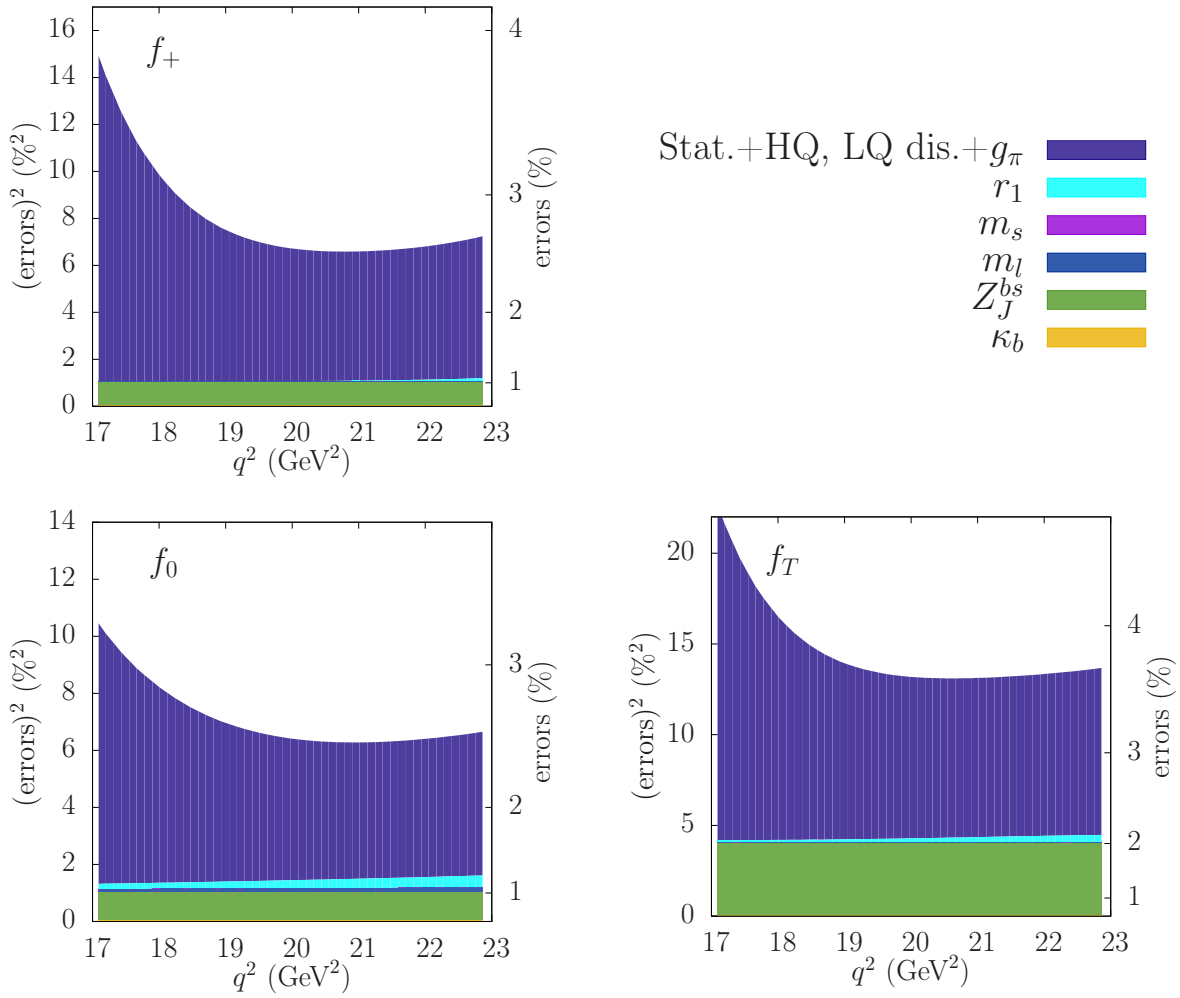

FIG. 11. Statistical and systematic error contributions to f_+ (upper left), f_0 (lower left), and f_T (lower right). The left vertical axis label shows the squares of the errors added in quadrature, while the right vertical axis label shows the errors themselves. The filled, stacked curves from bottom to top show the total error when we add each individual source of error in quadrature one-by-one.

G. Summary of the systematic error budget

Figure 11 visually summarizes the results for the statistical and systematic errors. For all three form factors, the combined chiral-continuum extrapolation error is the largest source of systematic uncertainty. The total errors in the form factors f_+, f_0, and f_T are below 5% for all $q^2 > 17$ GeV^2, and are $\sim 3\%$ near $q^2_{\rm max}$. We will quote numerical results for the form factors including all systematic errors over the entire q^2 range in the following section, after the q^2-extrapolation to the full kinematic range using the z expansion.

V. z EXPANSION OF FORM FACTORS

The form factors obtained from the chiral-continuum fit are reliable for high momentum transfer, $q^2 \gtrsim 17\ \mathrm{GeV}^2$. We only simulated kaons with momenta up to $2\pi(1,1,1)/L$, because, at higher momenta, the two- and three-point correlators become noisier and are subject to larger discretization errors. Further, the HMrSχPT formalism used to take the continuum limit does not apply when E_K is too large. In particular, for $E_K \gtrsim 1.2$ GeV the expansion parameter $\chi_E \gtrsim 1$, so the terms analytic in χ_E^n increase with higher powers of n. Because of these limitations, a way to extend the form factors to high kaon energy, or, equivalently, $q^2 = 0$, is needed. In this paper, we follow Ref. [31] and map q^2 to a new variable z such that $|z| \leq 1$. Constraints from unitarity, analyticity, and heavy-quark physics ensure that the expansion of the form factors in terms of z converges. Thus we can use the z expansion to obtain a model-independent parameterization of our form factors valid over the entire kinematic range. This technique is now standard for analyzing $B \to \pi l \nu$ decays [6, 120, 121].

We first define the new variable z via the conformal mapping [31]

$$z(q^2, t_0) = \frac{\sqrt{t_+ - q^2} - \sqrt{t_+ - t_0}}{\sqrt{t_+ - q^2} + \sqrt{t_+ - t_0}}, \tag{5.1}$$

where $t_\pm = (M_B \pm M_K)^2$ and t_0 is a free parameter that can be chosen to minimize $|z|$ for the semileptonic-decay region. In this work, we use $t_0 = (M_B + M_K)(\sqrt{M_B} - \sqrt{M_K})^2$ [33], which maps the physical semileptonic decay region $0 \leq q^2 \leq 22.8\ \mathrm{GeV}^2$ to $|z| < 0.15$. The small range of $|z|$ helps control the truncation error in the z expansion.

Using the new variable z, we expand the form factors as [33]

$$f_+(q^2) = \frac{1}{P_+(q^2)} \sum_{m=0}^{K-1} b_m^+ \left[z^m - (-1)^{m-K} \frac{m}{K} z^K \right], \tag{5.2}$$

$$f_0(q^2) = \frac{1}{P_0(q^2)} \sum_{m=0}^{K-1} b_m^0 z^m, \tag{5.3}$$

$$f_T(q^2) = \frac{1}{P_T(q^2)} \sum_{m=0}^{K-1} b_m^T \left[z^m - (-1)^{m-K} \frac{m}{K} z^K \right], \tag{5.4}$$

The function $P_{+,0,T}(q^2) = 1 - q^2/M^2$ accounts for poles below and near the B-K production threshold. For the z-fits of f_+ and f_T, we fix the location of the vector B_s^* pole to the measured value $M_{B_s^*} = 5.4154$ GeV [6]. For the f_0 fit, we fix the location of the scalar B_{s0}^* pole to the lattice-QCD prediction $M_{B_{s0}} = 5.711$ GeV from Ref. [112]. We find that varying

its location by three times the quoted theoretical error (±69 MeV) does not change the extrapolated form factor.

The expression for f_+ in Eq. (5.2) was derived by Bourrely, Caprini and Lellouch in Ref. [33], and is commonly called the BCL parameterization. In the BCL expression for f_+ in Eq. (5.2), the coefficient of the term proportional to z^K is related to that of the lower-order terms. This constraint is due to the conservation of momentum and the analyticity of the form factors [33]. There is no analogous constraint for f_0. We use the same expression for f_T as for f_+ because they are proportional to each other at leading order in the heavy-quark expansion. These expressions were also used to analyze the lattice form factors for $B \to K l^+ l^-$ in Refs. [21, 22].

Unitarity constrains the coefficients of the z expansion such that

$$\sum_{m,n=0}^{\infty} B_{mn} b_m b_n \lesssim 1, \tag{5.5}$$

where the values of B_{mn} are calculated using the Taylor expansion of the function discussed in Ref. [33] and given in Table X. We employ the same coefficients B_{mn} for f_T and f_+. The outer function ϕ defined in Ref. [122] is used in the derivation of the B_{mn}. Although the ϕ of f_0 in Ref. [122] was derived without a scalar pole, its form is not altered by the presence of the pole, because $|z|$ always equals 1 on the unit circle. In Ref. [122], Becher and Hill showed that, in the limit of large b-quark mass, the sizes of the z coefficients for f_+ are even smaller than the expectation from (5.5). Heavy-quark effective theory provides an estimate of the sum [122]:

$$\sum B_{mn} b_m b_n = \frac{1}{\pi} \int_{t_+}^{\infty} \frac{dt}{t - t_0} \mathrm{Im} \left(\sqrt{\frac{t_+ - t_0}{t_+ - t}} \right) |\phi_i(t) f_i(t)|^2, \tag{5.6}$$

where $i = +$, 0, or T, and the ϕ is outer function. To calculate the integral in Eq. (5.6), we need to know the form factors in the range $[t_+, \infty]$. For f_+, we assume that $f_\perp$ gives the dominant contribution and has only the single B_s^* pole. Taking the limit $M_B \to \infty$ gives the following simple form for $f_+(q^2)$:

$$f_+(q^2) \approx \frac{M_B}{\sqrt{2M_B}} f_\perp(E_K) \approx \frac{M_B}{\sqrt{2M_B}} \frac{C_\perp^{(0)} g_\pi}{f_\pi(E_K + \Delta_{B_s^*})}. \tag{5.7}$$

We then use our determination of $C_\perp^{(0)}$ from our preferred chiral-continuum fit to obtain the estimate

$$\sum B_{mn} b_m b_n \approx 0.012 \ . \tag{5.8}$$

TABLE X. Lowest-order coefficients B_{mn} for $B \to K l^+ l^-$ decay using $M_B = 5.27958$ GeV, $M_K = 0.497614$ GeV, and $t_0 = (M_B + M_K)(\sqrt{M_B} - \sqrt{M_K})^2$. The outer function used in the calculation is from Ref. [32] with $\chi_{f_+} = 5.025 \times 10^{-4}$ and $\chi_{f_0} = 1.4575 \times 10^{-2}$. Although these χ_is are derived for the $B \to \pi l \nu$ process, the calculation in the Ref. [34] shows the difference between χ_is of the $B \to K l^+ l^-$ and $B \to \pi l \nu$ process is less than 10%. Therefore, we quote the inputs from the Ref. [32] to obtain these B_{mn}. All B_{mn} not listed here can be obtained from the relations $B_{m(m+n)} = B_{0n}$ and $B_{mn} = B_{nm}$.

	B_{00}	B_{01}	B_{02}	B_{03}	B_{04}	B_{05}
$f_{+,T}$	0.0161	−0.0003	−0.0104	0.0002	0.0022	0.0002
f_0	0.0921	0.0132	−0.0483	−0.0168	−0.0001	0.0024

This result means the Eq. (5.5) is only a loose bound for f_+. In addition, it is consistent with a power-counting estimate [122], which anticipates $\sum B_{mn} b_m b_n$ to be of order $(\Lambda/m_b)^3$. The analogous calculation for f_T gives a similar result. The analysis below will show that the heavy-quark (HQ) constraint on f_+ (and f_T), Eq. (5.7), together with the kinematic constraint, $f_0(0) = f_+(0)$, suffices to keep the z fit under control.

We assume a log-normal distribution on $\sum B_{mn} b_m b_n$ to ensure that $\sum B_{mn} b_m b_n$ is always positive. The contribution from this prior to the augmented χ^2 is:

$$\chi^2_{B_{mn} b_m b_n} = \frac{\left[\ln(\sum B_{mn} b_m b_n) - \mu\right]^2}{\sigma^2}, \tag{5.9}$$

where μ is the central value and σ is the width of the prior. For f_+ and f_T, we choose μ and σ in Eq. (5.9) as $\ln(0.02)$ and $\ln(\frac{0.07}{0.02})$. This choice is conservative enough to accommodate the uncertainties in the estimates.

We first generate from the continuum, physical quark-mass limit of the chiral extrapolation a few synthetic data points in the energy range of the simulated lattice data ($q^2 \gtrsim 16.8$ GeV^2). With the lattice-spacing set to zero and the quark masses fixed to their physical values in the Eqs. (3.20) and (3.21), the physical form factors depend upon at most six independent functions of the kaon energy E_K. These are proportional to $1/(E_K + \Delta_{B_s^*})$, E_K^0, E_K, E_K^2, E_K^3, and E_K^4. To the degree that the coefficients in front of these functions are correlated, the number of independent modes may be even fewer than six. If we generate too many synthetic data points, the covariance matrix will be singular. We therefore generate

four synthetic data points each for f_+, f_0, and f_T at $q^2 = (22.86, 21.13, 19.17, 17.09)$ GeV^2. These cover the simulated lattice-momentum range and are approximately evenly spaced in q^2. We also fit with synthetic data from a smaller and larger range and find consistent results.

The full covariance matrix of the synthetic data points includes both the statistical and systematic error:

$$C_{mn}^{\rm full} = C_{mn}^{\rm stat} + C_{mn}^{\rm syst} \ , \tag{5.10}$$

where m, n denote the four q^2 values. The systematic error contribution is calculated as

$$C_{mn}^{\rm syst} = \sum_i \sigma_m^i \sigma_n^i \tag{5.11}$$

where the index i runs over the sources of systematic error discussed in Sec. IV. Because we assume that the systematic errors are 100% correlated between q^2 values, all nontrivial correlations between points are due to statistical fluctuations of the chiral-continuum fit results.

We first fit f_+, f_0, and f_T simultaneously in a combined fit using $K = 3$ (three free parameters) in Eqs. (5.2)–(5.4) without any constraints on the coefficients. Table XI presents the results of these fits. We plot the fit results in Fig. 12. Although we do not impose the kinematic condition $f_+(q^2 = 0) = f_0(q^2 = 0)$, it is approximately satisfied with separate fits. Adding HQ constraints on the f_+ and f_T fit makes the results even more consistent with the kinematic condition (see Fig. 12), and reduces the errors on f_+, f_T at low q^2. We then fit f_+, f_0, and f_T simultaneously with the kinematic constraint, and still including the HQ constraints on f_+ and f_T, which further decreases the extrapolation error in the form factors at low q^2. We implement the kinematic constraint by setting a prior of $f_+ - f_0$ at q^2=0 with central value zero and width of 0.00001.

We show the $\sum B_{mn} b_m b_n$ bootstrap distribution of f_+ and f_T from two fits with and without the HQ constraint in Fig. 13. Adding the HQ constraint moves the distribution of $\sum B_{mn} b_m b_n$ to smaller values. We also compare the $\sum B_{mn} b_m b_n$ distribution of f_0 from two fits in Fig. 14. One is a fit with f_0 only, the other is a combined f_+ and f_0 fit with the kinematic constraint. Adding the kinematic constraint decreases $\sum B_{mn} b_m b_n$ from the separate f_0 fit. Again, the result shows the unitary constraint on the $\sum B_{mn} b_m b_n$ of f_0 is a loose bound.

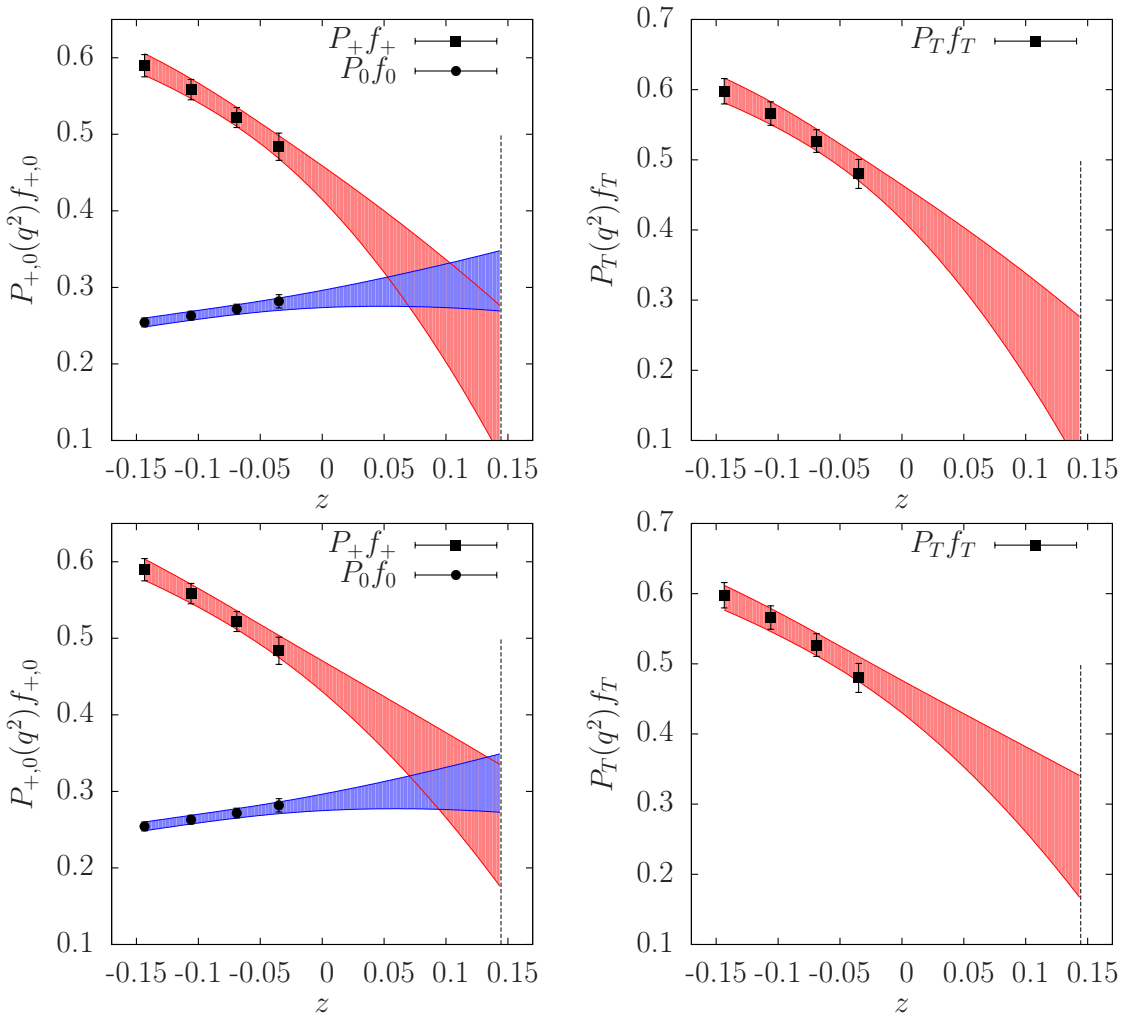

FIG. 12. Separate z-expansion fits of f_+, f_0 (left) and f_T (right) without (upper) and with (lower) HQ constraints on the sum of coefficients for f_+ and f_T. The synthetic data points are generated at large q^2 (small z) in the region of simulated lattice momenta. The kinematic condition $f_+(q^2=0) = f_0(q^2=0)$ is satisfied better when the HQ constraint is applied to f_+. (Recall that the factor $P_{+,0} = 1$ at $q^2 = 0$).

We also check the truncation error by repeating the fit with $K = 4$. Because in $K = 3$ fits, the coefficients b_2^i are not well determined by data, and the results are zero within error, we add a prior of 0(2) on b_4^i coefficients as in Ref. [21] to control the fluctuations of the higher order terms. All of the coefficients b from fits with $K = 3$ and 4 are summarized in Table XI. The results from different K are consistent with each other. The coefficients $b_{i,3}$ are zero within error and have little impact on the central value of the final result. We therefore conclude that the z truncation error is well controlled.

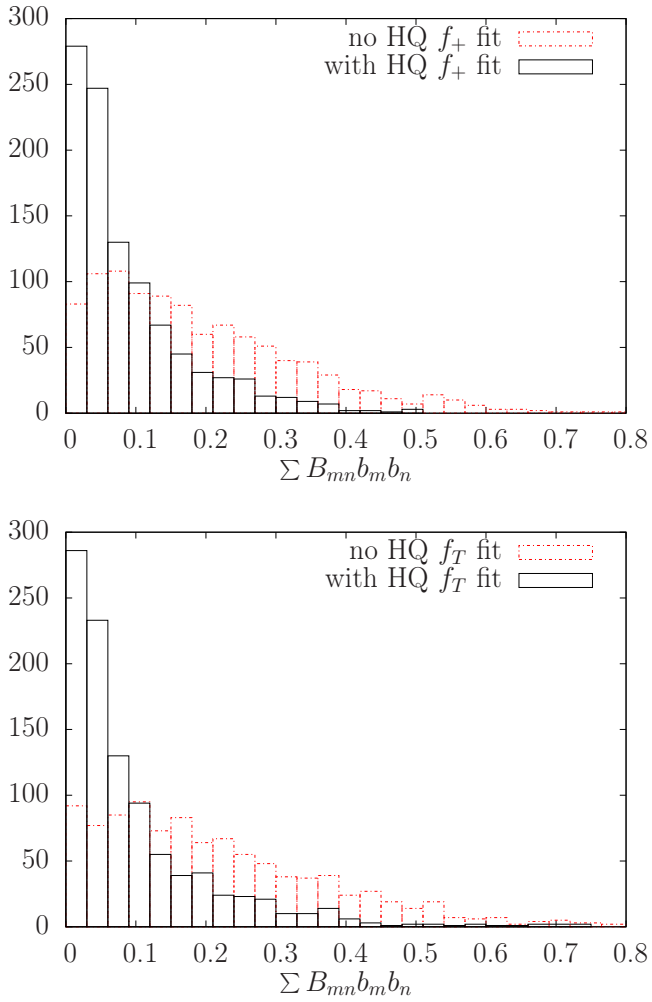

FIG. 13. Histogram of the the sum of coefficients $B_{mn}b_m b_n$ for f_+ and f_T from fits with and without the HQ constraint. Use of the HQ constraint moves the distribution of $B_{mn}b_m b_n$ to smaller values.

We record our final, preferred results from $K = 3$ z fits including both the heavy-quark and kinematic constraints in the third column of Table XI, and we give the corresponding correlation matrix in Table XII. Together with the pole masses (also in Table XI) and Eqs. (5.2)–(5.4), this information allows the reader to reconstruct our form-factor results throughout the full kinematic range. Our final form-factor results as a function of z and q^2 are plotted in Figs. 15 and 16.

VI. TESTS OF QCD PREDICTIONS FOR FORM-FACTOR RATIOS

Because lattice-QCD calculations of the $B \to K$ semileptonic form factors have until recently been unavailable, theoretical calculations of $B \to K l^+ l^-$ observables sometimes use

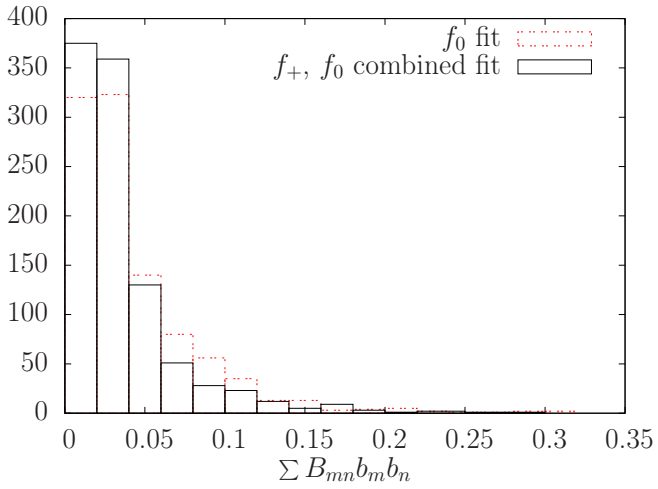

FIG. 14. Histogram of the sum of coefficients $\sum B_{mn} b_m b_n$ for f_0 from an independent fit and from a combined fit with f_+ that imposes the kinematic constraint at $q^2 = 0$.

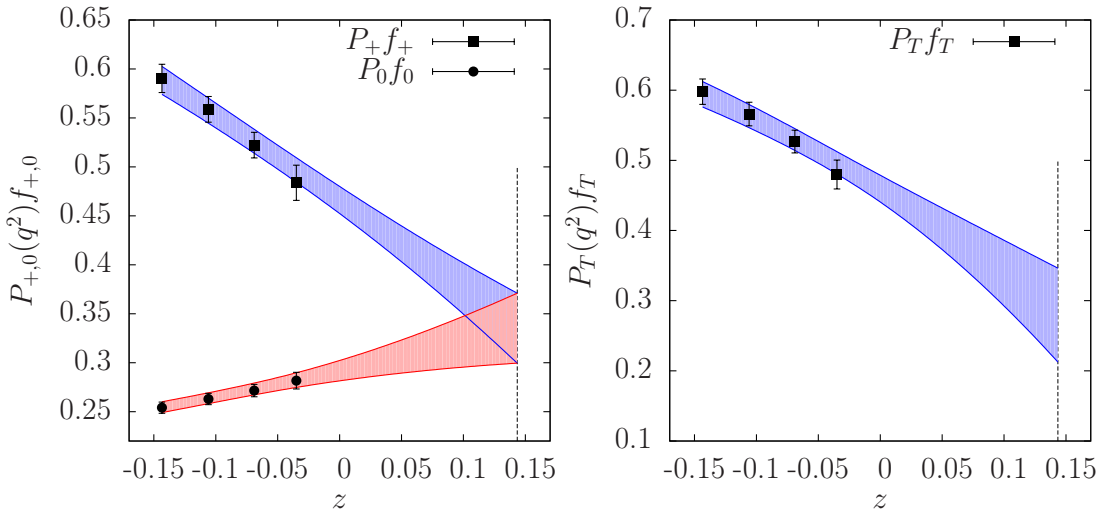

FIG. 15. f_+, f_0, and f_T z-expansion fits. The synthetic data points are generated at large q^2 (small z) from LECs of the HMrSχPT fit result. The kinematic constraint $f_+(q^2 = 0) = f_0(q^2 = 0)$ is applied exactly in the combined f_+ and f_0 z-expansion fit. The vertical dashed lines correspond to q^2=0. We use three coefficients ($K = 3$ in Eqs. (5.2)–(5.4)) for f_+, f_0, and f_T.

expectations from heavy-quark symmetries to relate them to others that can be constrained from experiment or computed with QCD models (see, e.g. Ref. [123]). Heavy-quark symmetry is also commonly used in phenomenological calculations of the related decays $B \to \pi l^+ l^-$, $B \to K^* l^+ l^-$, and $B \to K^* \gamma$ [39, 123–129]. Here we use our lattice-QCD form factors to directly test these heavy-quark symmetry relations in $B \to K$ decay at both high and low

TABLE XI. Results of z-expansion fits of the $B \to K$ form factors f_+ (top panel), f_0 (middle panel), and f_T (lower panel) using the formulae defined in Eqs. (5.2)–(5.4) with $t_0 = (M_B + M_K)(\sqrt{M_B} - \sqrt{M_K})^2$ [33], $M_{B_s^*} = 5.4154$ GeV in $f_{+,T}$, $M_{B_{s0}^*} = 5.711$ GeV in f_0, M_B=5.27958 GeV, and M_K = 0.497614 GeV [6].

	unconstrained	constrained		
		HQ	HQ + kinematic	
	$K = 3$	$K = 3$	$K = 3$	$K = 4$
b_0^+	0.437(22)	0.451(20)	0.466(14)	0.466(15)
b_1^+	-1.41(33)	-1.15(27)	-0.89(13)	-0.89(16)
b_2^+	-2.5(1.4)	-1.4(1.1)	-0.21(55)	-0.19(61)
b_3^+	–	–	–	0.3(1.1)
$\sum B_{mn} b_m b_n$	0.16	0.07	0.02	0.03
$f_+(0)$	0.18(10)	0.256(80)	0.335(36)	0.336(44)
b_0^0	0.285(11)	0.286(11)	0.292(10)	0.292(11)
b_1^0	0.19(14)	0.20(13)	0.28(12)	0.28(13)
b_2^0	-0.17(49)	-0.15(48)	0.15(44)	0.18(68)
b_3^0	–	–	–	0.2(1.7)
$\sum B_{mn} b_m b_n$	0.02	0.02	0.02	0.02
$f_0(0)$	0.309(39)	0.311(38)	0.335(36)	0.336(44)
b_0^T	0.440(25)	0.453(23)	0.460(19)	0.459(20)
b_1^T	-1.47(37)	-1.17(30)	-1.09(24)	-1.11(24)
b_2^T	-2.7(1.6)	-1.4(1.2)	-1.11(97)	-1.15(95)
b_3^T	–	–	–	-0.2(1.1)
$\sum B_{mn} b_m b_n$	0.18	0.07	0.05	0.05
$f_T(0)$	0.17(11)	0.254(87)	0.279(67)	0.276(68)
p value	0.57	0.39	0.34	0.97

q^2.

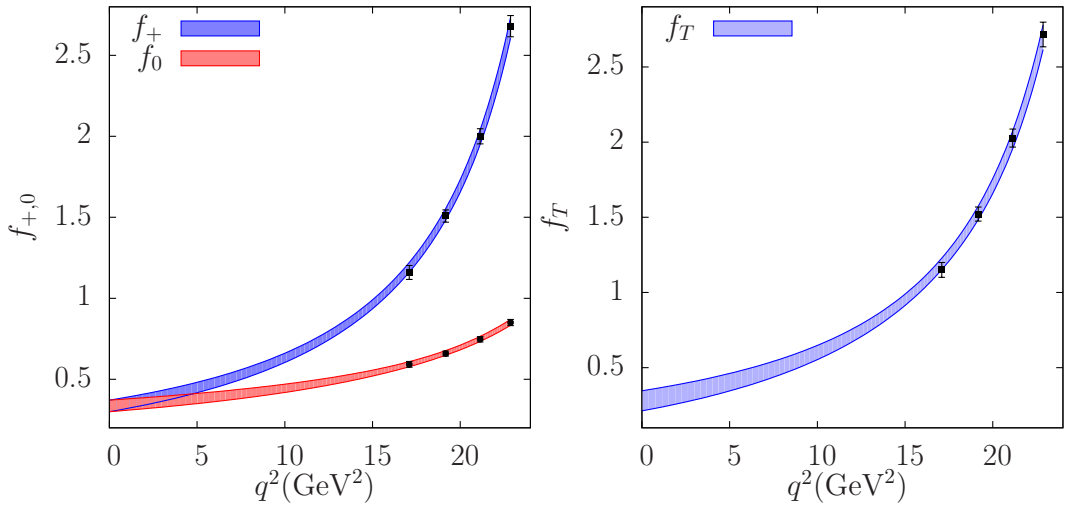

FIG. 16. f_+, f_0, and f_T vs. q^2 based on the z expansion. The kinematic constraint $f_+(q^2 = 0) = f_0(q^2 = 0)$ is applied exactly in the fit. We use three coefficients ($K = 3$ in Eqs. (5.2)–(5.2)) for f_+, f_0, and f_T.

TABLE XII. The coefficients b_i from the z-expansion fit (the first line) and their correlation matrix. The upper index $+$, 0, and T denote the form factors $f_{+,0,T}$. They are from the z-expansion fit formulae defined in Eqs. (5.2)–(5.4). We use $t_0 = (M_B + M_K)(\sqrt{M_B} - \sqrt{M_K})^2$ [33], $M_{B_s^*} = 5.4154$ GeV in $f_{+,T}$, $M_{B_{s0}^*} = 5.711$ GeV in f_0, M_B=5.27958 GeV and $M_K = 0.497614$ GeV [6].

	b_0^+	b_1^+	b_2^+	b_0^0	b_1^0	b_2^0	b_0^T	b_1^T	b_2^T
mean	0.466	-0.885	-0.213	0.292	0.281	0.150	0.460	-1.089	-1.114
error	0.014	0.128	0.548	0.010	0.125	0.441	0.019	0.236	0.971
b_0^+	1	0.450	0.190	0.857	0.598	0.531	0.752	0.229	0.117
b_1^+		1	0.677	0.708	0.958	0.927	0.227	0.443	0.287
b_2^+			1	0.595	0.770	0.819	-0.023	0.070	0.196
b_0^0				1	0.830	0.766	0.582	0.237	0.192
b_1^0					1	0.973	0.324	0.372	0.272
b_2^0						1	0.268	0.332	0.269
b_0^T							1	0.590	0.515
b_1^T								1	0.897
b_2^T									1

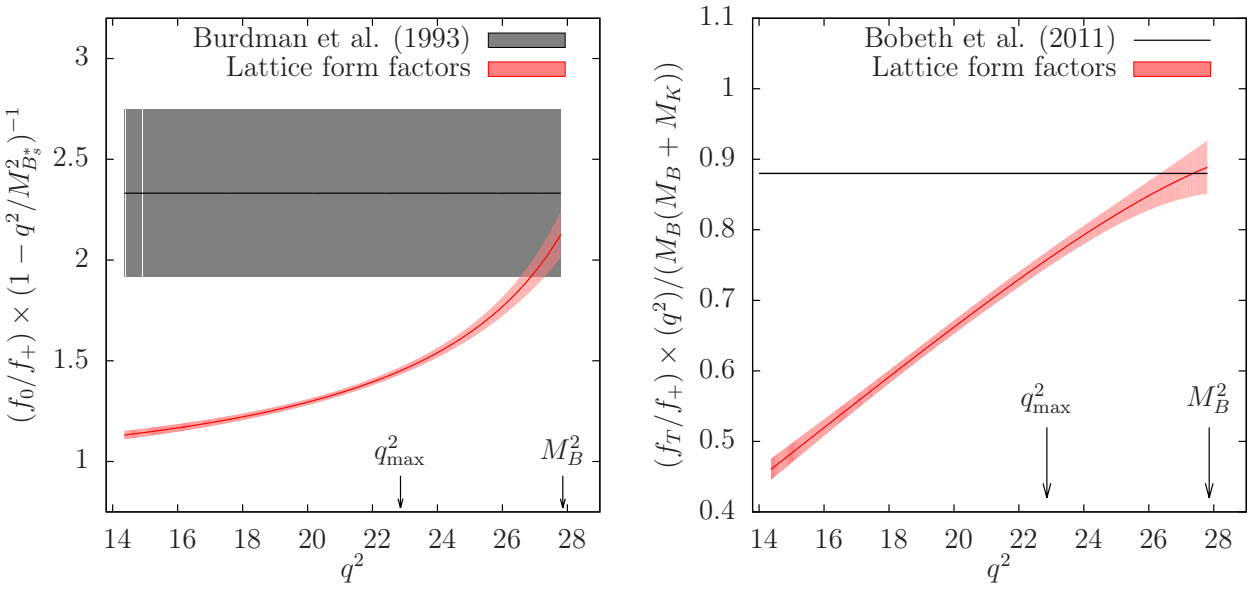

FIG. 17. Comparison of lattice form-factor ratios with theoretical predictions from heavy-quark symmetry at low recoil. Left: $(f_0/f_+)/(1 - q^2/M_{B_s^*}^2)^{-1}$ versus q^2 from lattice QCD (red curve with error band) and heavy-quark symmetry plus χPT [130] (gray horizontal band). The width of the theoretical band includes the uncertainty on $g_\pi = 0.45(8)$ but no other theory errors. Right: $(f_T/f_+) \times (q^2)/(M_B(M_B + M_K))$ versus q^2 from lattice QCD (red curve with error band) and the improved Isgur-Wise relation [123] (black horizontal line).

A. Low-recoil predictions from heavy-quark symmetry

In the soft-kaon ($E_K \ll M_B$) and chiral limits, the vector and scalar form factors can be related using heavy-quark effective theory and chiral perturbation theory [130, 131]:

$$\lim_{q^2 \to M_B^2} \frac{f_0}{f_+} = \left(\frac{f_{B_s}}{f_{B_s^*}}\right) \frac{1 - q^2/M_{B_s^*}^2}{g_\pi} + \mathcal{O}(\Lambda^2/m_b^2)\,, \tag{6.1}$$

where the decay-constant ratio accounts for heavy-quark corrections of $\mathcal{O}(1/m_b)$. Heavy-quark spin symmetry relates the vector and tensor form factors in the soft-kaon limit as [123, 132]:

$$\lim_{q^2 \to M_B^2} \frac{f_T}{f_+}(q^2, \mu) = \kappa(\mu) \frac{M_B(M_B + M_K)}{q^2} + \mathcal{O}(\Lambda/m_b)\,, \tag{6.2}$$

where the scale-dependent coefficient $\kappa(\mu)$ incorporates corrections of $\mathcal{O}(\alpha_s^2)$ to the leading Isgur-Wise relation [133] and is given in Eq. (2.5) of Ref. [123]. We can estimate the size of higher-order corrections in the heavy-quark expansion from power-counting. Taking $\Lambda = 500$ MeV and $m_b = 4.2$ GeV gives $\Lambda/m_b \sim 12\%$ and $(\Lambda/m_b)^2 \sim 1\%$. Equations (6.1)

and (6.2) also receive corrections from the kaon recoil energy that are of $\mathcal{O}(E_K/m_b)$. For $q^2_{\rm max} \geq q^2 \geq 14$ GeV^2, this ratio varies from $12\% \leq E_K/m_b \leq 40\%$, so such corrections are expected to be significant even at low kaon recoil.

Figure 17, left, compares the quantity $(f_0/f_+) \times (1 - q^2/M^2_{B^*_s})^{-1}$ obtained from our lattice form factors with the theoretical prediction Eq. (6.1). For the theoretical estimate, we take $f_{B^*_s}/f_{B_s} = 0.953(23)$ from the recent four-flavor lattice-QCD determination in Ref. [134] and $g_\pi = 0.45(8)$ as in our chiral-continuum fit. The width of the theoretical band is from the uncertainty on g_π, and does not include any other errors. Figure 17, right, compares the quantity $(f_T/f_+) \times (q^2)/(M_B(M_B + M_K))$ obtained from our lattice form factors with the theoretical prediction Eq. (6.2) using $m_b = 4.18$ GeV and $\alpha_{s\overline{\rm MS}}^{(4)}(m_b) = 0.2268$, such that $\kappa(m_b) \approx 0.88$ [123, 124]. We do not show any errors on the theoretical prediction.

The observed lattice form-factor ratios f_0/f_+ and f_T/f_+ at $q^2_{\rm max}$ are lower than the theoretical expectations by 38% and 15%, respectively; by $q^2 = 14.5$ GeV^2 the differences grow to 51% and 46%, respectively. Although the observed disagreement with the theoretical expectation for the tensor form-factor ratio is large, it is within the size expected (from simple power counting) for higher-order corrections due to the kaon recoil energy. The scalar form-factor ratio, however, differs from the theoretical expectation by a much larger amount. In Fig. 25 of Ref. [2] we compare the quantity $(f_0/f_+) \times (1 - q^2/M^2_{B^*_s})^{-1}$ for the related decay $B \to \pi l\nu$ with the heavy-quark prediction in the soft-pion limit. The observed agreement near $q^2_{\rm max}$ is better, which suggests that the discrepancy is indeed due to the light pseudoscalar-meson recoil energy, which is larger for $B \to K$ than for $B \to \pi$. Thus our lattice form-factor results suggest that one should be cautious in using heavy-quark relations derived in the soft-pion/kaon limit for phenomenological predictions, especially for decays with K or K^* final-state mesons.

B. Large-recoil predictions from QCD factorization

In the large-recoil limit ($E_K \gg M_K$), heavy-quark symmetry relates the vector, scalar, and tensor form factors to a single universal form factor [135]:

$$\lim_{E_K \gg M_K} \frac{f_0}{f_+} = \frac{2E_K}{M_B} + \mathcal{O}(\Lambda/m_b), \tag{6.3}$$

$$\lim_{E_K \gg M_K} \frac{f_T}{f_+} = \frac{M_B + M_K}{M_B} + \mathcal{O}(\Lambda/m_b). \tag{6.4}$$

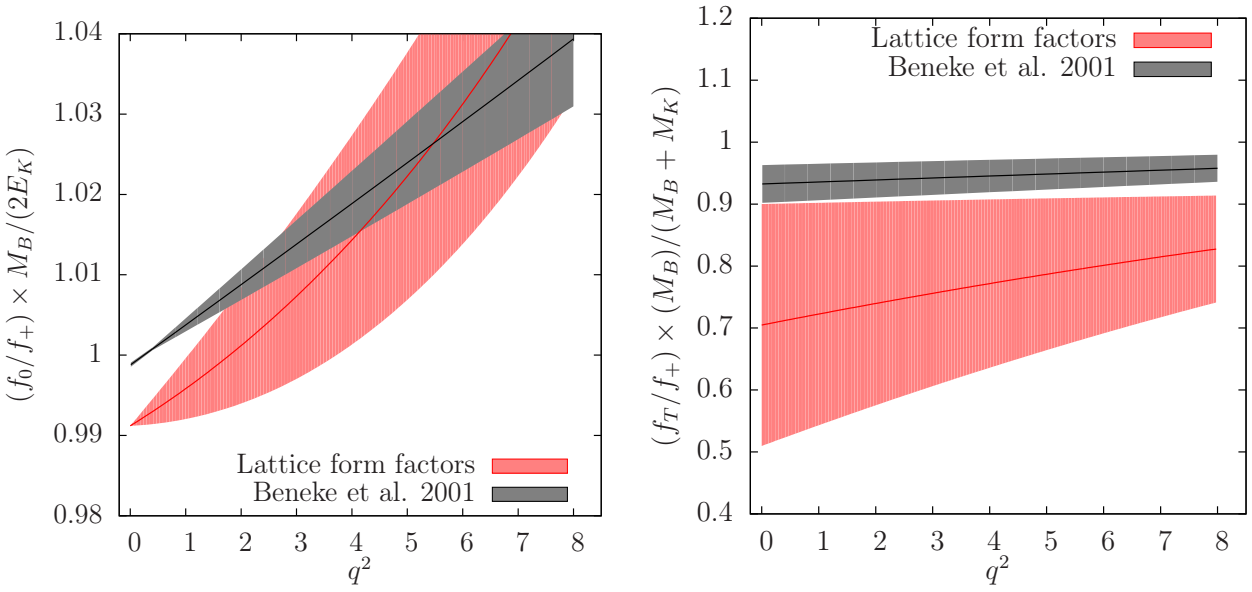

FIG. 18. Comparison of lattice form-factor ratios with theoretical predictions from heavy-quark symmetry at large recoil. Left: $(f_0/f_+) \times M_B/(2E_K)$ versus q^2 from lattice QCD (red curve with error band) and theoretical prediction with $\mathcal{O}(\alpha_s)$ corrections [136] (gray curve with error band). Right: $(f_T/f_+) \times (M_B)/(M_B + M_K)$ versus q^2 from lattice QCD (red curve with error band) and theoretical prediction with $\mathcal{O}(\alpha_s)$ corrections [136] (gray curve with error band).

The $\mathcal{O}(\alpha_s)$ corrections to these leading large-recoil expressions were derived using QCD factorization (QCDF) in Ref. [136], and the resulting expressions are given in Eqs. (62)–(63) of that work. Higher-order corrections in the heavy-quark expansion are expected to be about $\Lambda/m_b \sim 12\%$, while $\mathcal{O}(\alpha_s^2)$ corrections to the QCDF predictions from Ref. [136] are expected to be about 5%.

Figure 18 compares the lattice-form factor ratios with the theoretical large-recoil predictions from Ref. [136]. For the $\mathcal{O}(\alpha_s)$ corrections, we take the decay constants $f_B = 190.5(4.2)$ MeV from FLAG [121] and $f_K = 156.2(7)$ MeV from the PDG [6]. We take the first inverse moment of the B meson distribution amplitude $\lambda_B^{-1}(2.2\text{ GeV}) = [0.51(12)\text{ GeV}]^{-1}$ from LCSR [137], where the quoted theory error covers the spread of other determinations from QCD/light-cone sum rules and the operator product expansion [138–140]. We take the first and second moments of the kaon distribution amplitude $a_1^K(2\text{ GeV}) = 0.061(4)$ and $a_2^K(2\text{ GeV}) = 0.18(7)$ from a recent three-flavor lattice-QCD calculation [141]. We use our own determination of $f_+(q^2 = 0) = 0.335(36)$. We

take $\alpha_{s\overline{\rm MS}}^{(4)}(m_b) = 0.2268$ as described above and $\alpha_{s\overline{\rm MS}}^{(4)}(2.2\text{ GeV}) = 0.279$ [142]. The left panel of Fig. 18 shows the quantity $(f_0/f_+) \times (M_B)/(2E_K)$, while the right panel shows $(f_T/f_+) \times (M_B)/(M_B + M_K)$. The widths of the theoretical bands in Fig. 18 are from the uncertainty on λ_B^{-1} and $f_+(q^2 = 0)$, and do not include any other errors.

For $(f_0/f_+)\times M_B/(2E_K)$, the lattice-QCD result differs from the theoretical predictions by at most 1%, which is well within the expected size of heavy-quark corrections. For $(f_T/f_+)\times (M_B)/(M_B + M_K)$, the lattice-QCD result is marginally consistent with the theoretical expectation of Ref. [136]. A more recent NNLO calculation within soft-collinear effective theory (SCET) updates the large-recoil predictions to include $\mathcal{O}(\alpha_s^2)$ corrections [143]. The new $q^2 = 0$ result for $f_T/f_+ M_B/(M_B + M_K) = 0.817$ is in better agreement with the ratio obtained from lattice QCD. Overall, the uncertainty on the lattice-QCD tensor form-factor ratio at low q^2 is too large to draw any quantitative conclusions. (The vector and tensor form factors are not strongly correlated at low q^2.) Thus, while the scalar form-factor ratio suggests that the large-recoil predictions may be reliable, some caution is nevertheless warranted in their use for phenomenology given the limited number of tests they have undergone.

VII. SUMMARY AND OUTLOOK

As discussed in Sec. V, Table XII presents our final results for the form factors $f_+(q^2)$, $f_0(q^2)$, and $f_T(q^2)$ for the semileptonic process $B \to K l^+ l^-$. These entries, which consist of the coefficients of the BCL z expansion, Eqs. (5.2)–(5.4), together with the correlations among them, can be used to reconstruct our form factors with errors for all values of $0 \leq q^2 \leq q^2_{\rm max}$. This information can also be used to compute form-factor ratios and (differential) rates with squares of linear combinations of the form factors.

Figure 19 shows a comparison of our results with others in the literature. At $q^2 = 0$, our result is consistent with a light-cone-sum-rule result from Khodjamirian *et al.* [144]. For all q^2, our results are consistent with the only other unquenched lattice-QCD calculation from the HPQCD Collaboration [21]. Our form factors are somewhat more precise than HPQCD's, especially at high q^2, because we used more ensembles with finer lattice spacings and lighter quark masses. The total errors, including both statistical and systematic errors, are less than 4% at high q^2, and at low q^2 about 10% for f_+ and 30% for f_T.

More generally, our results can be used to compute any $B \to Kll$ observable, including asymmetries and decay rates, for all possible dilepton final states ($l = \ell, \tau, \nu$), and even lepton-flavor-violating modes [145]. We present a thorough analysis of observables for $B \to K$ semileptonic decays in a companion publication [146], where we also present ratios of observables for $B \to Kll$ to $B \to \pi ll$ decay processes. The three form factors f_+, f_0, and f_T suffice to parameterize the factorizable hadronic contributions to $B \to K$ semileptonic decays in any extension of the Standard Model. Other hadronic uncertainties, such as violations of quark-hadron duality due to intermediate charmonium resonances, must, of course, also be reliably estimated to obtain complete Standard-Model and new-physics predictions for $B \to K$ processes. If deviations from the Standard Model are observed in any $B \to Kll$ decay channel, accurate results for the form factors will be essential to disentangling the underlying physics.

The main sources of uncertainty in our form factors are from the chiral-continuum extrapolation and extrapolation to low q^2. We plan to reduce these uncertainties with newer gauge-field ensembles that are being generated by the MILC Collaboration [147, 148]. These ensembles use the highly-improved staggered quark (HISQ) action for the light, strange, and charm quarks. This action is designed to have smaller discretization effects which will help reduce the size of the continuum extrapolation errors [149]. In addition, the HISQ ensembles include ensembles with physical pion masses, which will eliminate the need for the chiral

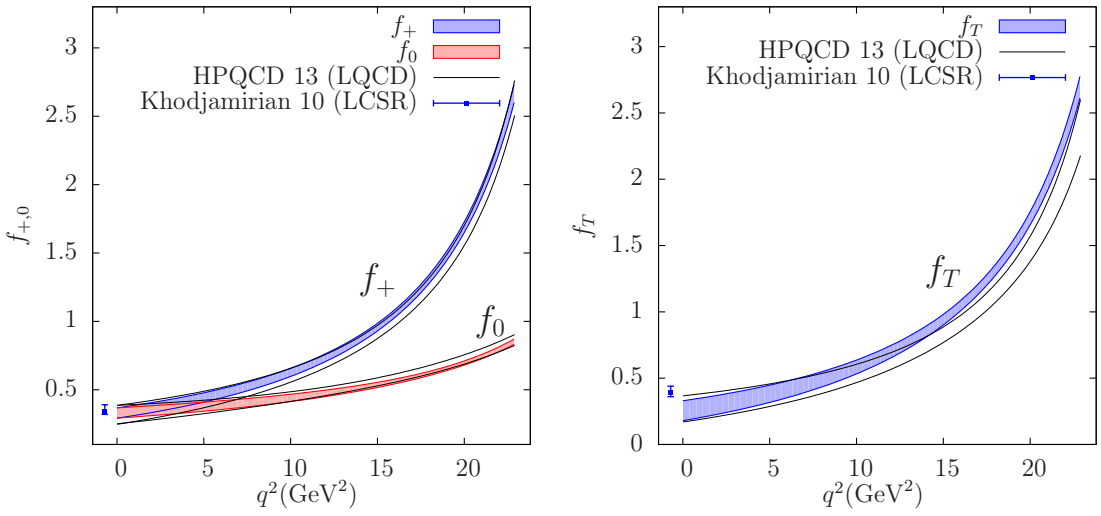

FIG. 19. Our form factors compared with light-cone sum rule results [144] and the other unquenched lattice-QCD calculation [21].

extrapolation and the associated errors. Indeed, these ensembles have already been used to improve the precision for kaon [150] and charmed-meson [151] physics. In particular, we found with D- and D_s-meson decay constants [151] that an analysis with physical and unphysical quark masses provides better statistical precision with no penalty in systematic errors.

ACKNOWLEDGMENTS

We thank Wolfgang Altmannshofer, Martin Beneke, and Enrico Lunghi for useful conversations about the form factors and phenomenology of $b \to s$ processes. We thank Heechang Na for useful conversations about correlator fit techniques. We thank Richard J. Hill for clarifying discussions about the unitarity constraints in the z-expansion. Computations for this work were carried out with resources provided by the USQCD Collaboration, the Argonne Leadership Computing Facility, the National Energy Research Scientific Computing Center, and the Los Alamos National Laboratory, which are funded by the Office of Science of the U.S. Department of Energy; and with resources provided by the National Institute for Computational Science, the Pittsburgh Supercomputer Center, the San Diego Supercomputer Center, and the Texas Advanced Computing Center, which are funded through the National Science Foundation's Teragrid/XSEDE Program. This work was supported in part by the U.S. Department of Energy under Grants No. DE-FG02-91ER40628 (C.B., J.K.), No. DE-FC02-12ER41879 (C.D., J.F., L.L.), No. DE-FG02-91ER40661 (S.G., R.Z.), No. DE-SC0010120 (S.G.), No. DE-FC02-06ER41443 (R.Z.), No. DE-FG02-91ER40677 (A.X.K.,C.M.B.,D.D.,E.D.F.,R.D.J.), No. DE-FG02-13ER42001 (A.X.K.,D.D.) No. DE-FG02-ER41976 (D.T.); No. DE-SC0010114 (Y.L., Y.M.); by the National Science Foundation under Grants No. PHY-0555243, No. PHY-0757333, No. PHY10-67881 (C.D., L.L.), No. PHY-1316748 (R.S.), No. PHY-1212389 (R.Z.), No. PHY-1417805 (J.L., D. D.); by the URA Visiting Scholars' program, (Y.L., Y.M., A.X.K., D.D., C.M.B.); by the MICINN (Spain) under grant FPA2010-16696 and Ramón y Cajal program (E.G.); by the Junta de Andalucía (Spain) under Grants No. FQM-101 and No. FQM-6552 (E.G.); by European Commission (EC) under Grant No. PCIG10-GA-2011-303781 (E.G.); by the German Excellence Initiative and the European Union Seventh Framework Programme under grant agreement No. 291763 as well as the European Union's Marie Curie COFUND program

(A.S.K.); and by the Basic Science Research Program of the National Research Foundation of Korea (NRF) funded by the Ministry of Education (No. 2014027937) and the Creative Research Initiatives Program (No. 2014001852) of the NRF grant funded by the Korean government (MEST) (J.A.B.). This manuscript has been co-authored by an employee of Brookhaven Science Associates, LLC, under Contract No. DE-AC02-98CH10886 with the U.S. Department of Energy. Fermilab is operated by Fermi Research Alliance, LLC, under Contract No. DE-AC02-07CH11359 with the United States Department of Energy.

Appendix A: $B \to Kll$ form factors in SU(2) SχPT

We use expressions derived in Heavy Meson Rooted Staggered χPT (HMrSχPT) [106] as the low-energy effective theory of QCD in which the degrees-of-freedom are pions and kaons for our chiral-continuum extrapolations. SU(3) HMrSχPT [106, 152, 153] was applied to $B \to \pi l\nu$ semileptonic decays [1]. More recently, SU(2) HMχPT [118, 154, 155] was also considered as an alternative effective theory in studies of heavy meson physics. We derive the SU(2) HMrSχPT formulae for form factors calculated with staggered quarks in this appendix. These formulae can be used for $B \to \pi l\nu$, $B \to K l^+ l^-$ and D meson semileptonic decays. Our results are consistent with earlier studies of HMχPT for continuum QCD and Wilson quarks [155] after taking the continuum limit of the HMrSχPT expressions. The differences in the detailed expressions can be absorbed into redefinitions of the scale or low-energy constants (LECs).

1. $f_\parallel$ and $f_\perp$ in SU(3) HMrSχPT

The SU(3) HMrSχPT expression of $f_\parallel$ is the same as in Eq. (3.20). We only list the expression of the log terms for unitary points ($m_{l,h} = m'_{l,h} = m_{l,s}$) here.

For the $B \to \pi$ process, the chiral logs in SU(3) HMrSχPT are given by [106]:

$$\begin{aligned}
\text{logs}^{B\to\pi}_{\parallel,\text{SU(3)}} = \frac{1}{(4\pi f)^2}\Bigg\{ & \frac{1}{16}\sum_{\Xi}\Bigg[\frac{1-3g_\pi^2}{2}\left[2I_1(m_{\pi,\Xi}) + I_1(m_{K,\Xi})\right] \\
& + 2I_2(m_{\pi,\Xi}, E) + I_2(m_{K,\Xi}, E)\Bigg] \\
& + \frac{1+3g_\pi^2}{4}\left[I_1(m_{\pi,I}) - \frac{1}{3}I_1(m_{\eta,I})\right] \\
& + \sum_{j\in\{\pi,\eta,\eta'\}}\Bigg[a^2\delta'_V R_j^{[3,1]}\left(\{m_{\pi,V}, m_{\eta,V}, m_{\eta',V}\}; \{m_{S,V}\}\right) \times \\
& \left(\frac{3(g_\pi^2-1)}{2}I_1(m_{j,V}) - 2I_2(m_{j,V}, E)\right)\Bigg] + [V \to A]\Bigg\}.
\end{aligned} \tag{A1}$$

For the $B \to K$ process, the chiral logs in SU(3) HMrSχPT are given by:

$$\begin{aligned}
\text{logs}^{B\to K}_{\parallel,\text{SU(3)}} = \frac{1}{(4\pi f)^2}\Bigg\{ & \frac{1}{16}\sum_{\Xi}\Bigg[\frac{2-3g_\pi^2}{2}I_1(m_{K,\Xi}) - 3g_\pi^2 I_1(m_{\pi,\Xi}) + \frac{1}{2}I_1(m_{S,\Xi}) \\
& + 2I_2(m_{K,\Xi}, E) + I_2(m_{S,\Xi}, E)\Bigg] \\
& - \frac{1}{2}I_1(m_{S,I}) + \frac{3g_\pi^2}{4}I_1(m_{\pi,I}) + \frac{8-3g_\pi^2}{12}I_1(m_{\eta,I}) + I_2(m_{\eta,I}, E) - I_2(m_{S,I}, E) \\
& + a^2\delta'_V\Bigg[\frac{I_1(m_{\eta',V}) - I_1(m_{\eta,V}) + I_2(m_{\eta',V}, E) - I_2(m_{\eta,V}, E)}{m^2_{\eta',V} - m^2_{\eta,V}} \\
& - \sum_{j\in\{S,\eta,\eta'\}} R_j^{[3,1]}\left(\{m_{S,V}, m_{\eta,V}, m_{\eta',V}\}; \{m_{\pi,V}\}\right)\left(\frac{1}{2}I_1(m_{j,V}) + I_2(m_{j,V}, E)\right) \\
& + \frac{3g_\pi^2}{2}\sum_{j\in\{\pi,\eta,\eta'\}} R_j^{[3,1]}\left(\{m_{\pi,V}, m_{\eta,V}, m_{\eta',V}\}; \{m_{S,V}\}\right) I_1(m_{j,V})\Bigg] \\
& + [V \to A]\Bigg\}.
\end{aligned} \tag{A2}$$

The masses and integrals that appear in Eqs. (A1) and (A2) are as follows. The flavor off-diagonal meson masses are:

$$m^2_{\pi,\Xi} = \mu(m_l + m_l) + a^2\Delta_\Xi, \tag{A3}$$

$$m^2_{K,\Xi} = \mu(m_l + m_s) + a^2\Delta_\Xi, \tag{A4}$$

$$m^2_{S,\Xi} = \mu(m_s + m_s) + a^2\Delta_\Xi, \tag{A5}$$

where m_l and m_s are sea quark masses and the taste label Ξ has values P, V, T, A and I.

The masses of flavor-neutral mesons in the taste vector channel are [156]:

$$m^2_{\pi^0,V} = m^2_{U,V} = m^2_{D,V} = \mu(m_l + m_l) + a^2\Delta_V, \tag{A6}$$

$$m^2_{S,V} = \mu(m_s + m_s) + a^2\Delta_V, \tag{A7}$$

$$m^2_{\eta,V} = \frac{1}{2}\left(m^2_{U_V} + m^2_{S_V} + \frac{3}{4}a^2\delta'_V - Z\right), \tag{A8}$$

$$m^2_{\eta',V} = \frac{1}{2}\left(m^2_{U,V} + m^2_{S,V} + \frac{3}{4}a^2\delta'_V + Z\right), \tag{A9}$$

$$Z \equiv \sqrt{\left(m^2_{S,V} - m^2_{U,V}\right)^2 - \frac{a^2\delta'_V}{2}\left(m^2_{S,V} - m^2_{U,V}\right) + \frac{9(a^2\delta'_V)^2}{16}}. \tag{A10}$$

The taste-axial case just requires substituting A for V. For the taste-singlet case, we have:

$$m^2_{\pi^0,I} = m^2_{U,I} = m^2_{D,I} = \mu(m_l + m_l) + a^2\Delta_I, \tag{A11}$$

$$m^2_{S,I} = \mu(m_h + m_h) + a^2\Delta_I, \tag{A12}$$

$$m^2_{\eta,I} = \frac{m^2_{U,I}}{3} + \frac{2m^2_{S,I}}{3}, \tag{A13}$$

$$m^2_{\eta',I} = m^2_0. \tag{A14}$$

The momentum integrals I_1 and I_2 that appear in the chiral log terms are defined as:

$$I_1(m) = m^2 \ln\left(\frac{m^2}{\Lambda^2}\right), \tag{A15}$$

$$I_2(m,\Delta) = -2\Delta^2 \ln\left(\frac{m^2}{\Lambda^2}\right) - 4\Delta^2 F\left(\frac{m}{\Delta}\right) + 2\Delta^2, \tag{A16}$$

$$F(x) = \begin{cases} \sqrt{1-x^2}\tanh^{-1}\left(\sqrt{1-x^2}\right) & 0 \le x \le 1, \\ -\sqrt{x^2-1}\tan^{-1}\left(\sqrt{x^2-1}\right) & x \ge 1, \end{cases} \tag{A17}$$

where Λ is the renormalization scale.

Similarly, $f_\perp$ on the unitary points in NLO SU(3) HMrSχPT is given by [106]:

$$\begin{aligned} f_\perp = {} & \frac{C^{(0)}}{f}\left[\frac{1}{E + \Delta^*_B + D}\right] \\ & + \frac{C^{(0)}}{f(E + \Delta_{B^*})}(\text{logs} + C^{(1)}\chi_l + C^{(2)}\chi_s + C^{(3)}\chi_E + C^{(4)}\chi^2_E + C^{(5)}\chi_{a^2}), \end{aligned} \tag{A18}$$

where $\Delta_{B^*_s} = M_{B^*_s} - M_B$. (The SU(3) expression has one extra chiral log term D comparing with the SU(2) expression we used in our analysis.) There are two chiral log related terms parameterized by D and logs in Eq. (A18). For the $B \to \pi$ process, the SU(3) expressions

are [106]:

$$D^{B\to\pi}_{\mathrm{SU(3)}} = -\frac{3g_\pi^2 E}{(4\pi f)^2}\Bigg\{\frac{1}{16}\sum_{\Xi}\left[2J_1^{\mathrm{sub}}(m_{\pi,\Xi},E)+J_1^{\mathrm{sub}}(m_{K,\Xi},E)\right] - \frac{1}{2}J_1^{\mathrm{sub}}(m_{\pi,I},E)+\frac{1}{6}J_1^{\mathrm{sub}}(m_{\eta,I},E) + \sum_{j\in\{\pi,\eta,\eta'\}}\left[(-a^2\delta'_V)R_j^{[3,1]}\left(\{m_{\pi,V},m_{\eta,V},m_{\eta',V}\};\{m_{S,V}\}\right)J_1^{\mathrm{sub}}(m_{j,V},E)\right] + \left[V\to A\right]\Bigg\}, \tag{A19}$$

and

$$\mathrm{logs}^{B\to\pi}_{\perp,\mathrm{SU(3)}} = \frac{1}{(4\pi f)^2}\Bigg\{\frac{1}{16}\sum_{\Xi}\left[-\frac{1+3g_\pi^2}{2}\left[2I_1(m_{\pi,\Xi})+I_1(m_{K,\Xi})\right]\right] -\frac{1}{2}g_\pi^2 J_1^{\mathrm{sub}}(m_{\pi,I},E)+\frac{1}{6}g_\pi^2 J_1^{\mathrm{sub}}(m_{\eta,I},E)+\frac{1+3g_\pi^2}{12}\left[3I_1(m_{\pi,I})-I_1(m_{\eta,I})\right] + \sum_{j\in\{\pi,\eta,\eta'\}}\Bigg[a^2\delta'_V R_j^{[3,1]}\left(\{m_{\pi,V},m_{\eta,V},m_{\eta',V}\};\{m_{S,V}\}\right) \times\left(g_\pi^2 J_1^{\mathrm{sub}}(m_{j,V},E)+\frac{1+3g_\pi^2}{2}I_1(m_{j,V})\right)\Bigg]+[V\to A]\Bigg\}. \tag{A20}$$

For the $B\to K$ process, the SU(3) expressions are:

$$D^{B\to K}_{\mathrm{SU(3)}} = -\frac{3g_\pi^2(E)}{(4\pi f)^2}\Bigg\{\frac{1}{16}\sum_{\Xi}\left[2J_1^{\mathrm{sub}}(m_{K,\Xi},E)+J_1^{\mathrm{sub}}(m_{S,\Xi},E)\right] + \frac{2}{3}J_1^{\mathrm{sub}}(m_{\eta,I},E)-J_1^{\mathrm{sub}}(m_{S,I},E) + \sum_{j\in\{S,\eta,\eta'\}}\left[(-a^2\delta'_V)R_j^{[3,1]}\left(\{m_{S,V},m_{\eta,V},m_{\eta',V}\};\{m_{\pi,V}\}\right)J_1^{\mathrm{sub}}(m_{j,V},E)\right] + \left[V\to A\right]\Bigg\}, \tag{A21}$$

and

$$\begin{aligned}\text{logs}^{B\to K}_{\perp,\text{SU(3)}} = \frac{1}{(4\pi f)^2}\Bigg\{ & \frac{1}{16}\sum_{\Xi}\left[-\frac{2+3g_\pi^2}{2}I_1(m_{K,\Xi}) - \frac{1}{2}I_1(m_{S,\Xi}) - 3g_\pi^2 I_1(m_{\pi,\Xi})\right] \\ & -\frac{1}{3}g_\pi^2 J_1^{\text{sub}}(m_{\eta,I},E) + \frac{3g_\pi^2}{4}I_1(m_{\pi,I}) - \frac{4+3g_\pi^2}{12}I_1(m_{\eta,I}) + \frac{1}{2}I_1(m_{S,I}) \\ & + a^2\delta_V'\Bigg[\frac{g_\pi^2}{m_{\eta',V}^2 - m_{\eta,V}^2}\left(J_1^{\text{sub}}(m_{\eta,V},E) - J_1^{\text{sub}}(m_{\eta',V},E)\right) \\ & + \frac{3g_\pi^2}{2}\sum_{j\in\{\pi,\eta,\eta'\}} R_j^{[3,1]}\left(\{m_{\pi,V},m_{\eta,V},m_{\eta',V}\};\{m_{S,V}\}\right) I_1(m_{j,V}) \\ & + \frac{1}{2}\sum_{j\in\{S,\eta,\eta'\}} R_j^{[3,1]}\left(\{m_{S,V},m_{\eta,V},m_{\eta',V}\};\{m_{\pi,V}\}\right) I_1(m_{j,V})\Bigg] \\ & + [V\to A]\Bigg\}\,. \end{aligned} \tag{A22}$$

The definition of the meson mass terms and I_1 are the same as for the $f_\parallel$ case. The $f_\perp$ expression has an extra function J_1, that is defined as:

$$J_1(m,\Delta) = \left(-m^2 + \frac{2}{3}\Delta^2\right)\ln\left(\frac{m^2}{\Lambda^2}\right) + \frac{4}{3}(\Delta^2 - m^2)F\left(\frac{m}{\Delta}\right) - \frac{10}{9}\Delta^2 + \frac{4}{3}m^2\,, \tag{A23}$$

$$J_1^{\text{sub}}(m,\Delta) \equiv J_1(m,\Delta) - \frac{2\pi m^3}{3\Delta}\,. \tag{A24}$$

2. $f_\parallel$ and $f_\perp$ in SU(2) HMrSχPT

We derive the SU(2) formula for $f_\parallel$ and $f_\perp$ based on the SU(3) expression. We also use the same expression for f_T as for $f_\perp$ as discussed in Sec. III D. To obtain the SU(2) limit of an SU(3) expression, we treat the strange quark mass as infinitely heavy. The SU(2) form does not contain m_s explicitly, but all LECs depend implicitly on m_s. Because our lattice data have slightly different m_s on different ensembles, we keep the analytic term which is proportional to m_s. Next, we consider all terms in the SU(3) chiral log expression. If a term is proportional to m_s or $\ln m_s$ in the large m_s limit, it is absorbed into the redefinition of other LECs. If a term is proportional to $1/m_s$ or $1/\ln m_s$ in the large m_s limit, it does not appear in the SU(2) expression. We now derive the form of the chiral log terms in the SU(2) limit.

For the chiral log terms in $f_\parallel$, because we take m_s to infinity, all m_s related terms, such as $m_{K,\Xi}$, $m_{S,\Xi}$, $m_{\eta,I}$ and $m_{\eta',V/A/I}$ go to infinity. They are absorbed into LECs. Only $m_{\eta,V/A}$ is finite and goes like $\sqrt{m_U^2 + \frac{\delta'_{V/A}}{2}}$. We now consider all contributing chiral log terms.

- $I_1(m)$ goes like $m^2 \ln m^2$, so only $I_1(M_\pi)$ survives.
- $I_2(m, E)$ diverges as $2\pi m E$ when $m \to \infty$, so only $I_2(M_\pi, E)$ survives.
- The ratio
$$\frac{I_1(m_{\eta',V}) - I_1(m_{\eta,V}) + I_2(m_{\eta',V}, E) - I_2(m_{\eta,V}, E)}{m^2_{\eta',V} - m^2_{\eta,V}},$$
diverges as $2 \ln m_s$ at large m_s, so it is removed.
- We find that
$$\lim_{m_s \to \infty} a^2 \delta'_{V/A} R_j^{[3,1]} \left(\{m_{S,V}, m_{\eta,V}, m_{\eta',V}\}; \{m_{\pi,V}\} \right) = \begin{cases} 4, & j = S \\ -\frac{a^4 \delta'^2_{V/A}}{2 m_S^4} = 0, & j = \eta \\ -4, & j = \eta', \end{cases} . \quad \text{(A25)}$$
When this term multiplies I_1 or I_2, it is divergent as $m_s \to \infty$ for $j = S$ or $j = \eta'$. For $j = \eta$, the I_1 and I_2 are finite, but the total contribution is zero as $m_s \to \infty$. So these terms are removed.
- We find that
$$\lim_{m_s \to \infty} a^2 \delta'_{V/A} R_j^{[3,1]} \left(\{m_{\pi,V}, m_{\eta,V}, m_{\eta',V}\}; \{m_{S,V}\} \right) = \begin{cases} 2, & j = \pi \\ -2, & j = \eta \\ -\frac{a^4 \delta'^2_{V/A}}{4 m_S^4} = 0, & j = \eta' \end{cases} , \quad \text{(A26)}$$
so only $j = \pi$ and $j = \eta$ terms contribute in the SU(2) theory.

In summary, for the $B \to \pi$ process, the chiral log in SU(2) HMrSχPT is given by

$$\begin{aligned} \text{logs}^{B\to\pi}_{\parallel,\text{SU}(2)} = \frac{1}{(4\pi f)^2} \Bigg\{ & \frac{1}{16} \sum_{\Xi} \left[(1 - 3g_\pi^2) I_1(m_{\pi,\Xi}) + 2 I_2(m_{\pi,\Xi}, E) \right] + \frac{1 + 3g_\pi^2}{4} I_1(m_{\pi,I}) \\ & + 2 \left[\frac{3(g_\pi^2 - 1)}{2} I_1(m_{\pi,V}) - 2 I_2(m_{\pi,V}, E) \right] - 2 \left[\frac{3(g_\pi^2 - 1)}{2} I_1(m_{\eta,V}) - 2 I_2(m_{\eta,V}, E) \right] \\ & + [V \to A] \Bigg\} . \end{aligned} \quad \text{(A27)}$$

For the $B \to K$ process, the chiral log in SU(2) HMrSχPT is given by

$$\begin{aligned} \text{logs}^{B\to K}_{\parallel,\text{SU}(2)} = \frac{1}{(4\pi f)^2} \Bigg\{ & \frac{1}{16} \sum_{\Xi} \left[-3 g_\pi^2 I_1(m_{\pi,\Xi}) \right] + \frac{3 g_\pi^2}{4} I_1(m_{\pi,I}) \\ & + \frac{3 g_\pi^2}{2} \left[2 I_1(m_{\pi,V}) - 2 I_1(m_{\eta,V}) \right] + [V \to A] \Bigg\} . \end{aligned} \quad \text{(A28)}$$

We then derive the expression for the $f_\perp$ chiral log terms in SU(2) HMrSχPT. We use the same treatment of analytic terms as was done for $f_\parallel$. To calculate the SU(2) chiral log terms, we consider the large m_s limit of J_1:

$$\lim_{m\to\infty} J_1(m,E) \to -m^2 \ln m^2 \to -\infty, \tag{A29}$$

$$\lim_{m_s\to\infty} \frac{J_1^{\rm sub}(m_{\eta,V},E) - J_1^{\rm sub}(m_{\eta',V},E)}{m_{\eta',V}^2 - m_{\eta,V}^2} \to 2\ln m_s \to \infty. \tag{A30}$$

So all J_1 related terms are absorbed into the redefinition of LECs and disappear.

Via a procedure similar to that for $f_\parallel$, we obtain the SU(2) chiral log terms in $f_\perp$ for the $B\to\pi$ channel:

$$\begin{aligned} D_{\rm SU(2)}^{B\to\pi} = -\frac{3g_\pi^2 E}{(4\pi f)^2}\Bigg\{ & \frac{1}{16}\sum_\Xi \left[2J_1^{\rm sub}(m_{\pi,\Xi},E)\right] - \frac{1}{2}J_1^{\rm sub}(m_{\pi,I},E) \\ & - \left[2J_1^{\rm sub}(m_{\pi,V},E) - 2J_1^{\rm sub}(m_{\eta,V},E)\right] + [V\to A]\Bigg\}, \end{aligned} \tag{A31}$$

$$\begin{aligned} {\rm logs}_{\perp,{\rm SU(2)}}^{B\to\pi} = \frac{1}{(4\pi f)^2}\Bigg\{ & \frac{1}{16}\sum_\Xi \left[-\frac{1+3g_\pi^2}{2}\left[2I_1(m_{\pi,\Xi})\right]\right] - \frac{1}{2}g_\pi^2 J_1^{\rm sub}(m_{\pi,I},E) \\ & + \frac{1+3g_\pi^2}{12}\left[3I_1(m_{\pi,I})\right] + \Bigg[2\left(g_\pi^2 J_1^{\rm sub}(m_{\pi,V},E) + \frac{1+3g_\pi^2}{2}I_1(m_{\pi,V})\right) \\ & - 2\left(g_\pi^2 J_1^{\rm sub}(m_{\eta,V},E) + \frac{1+3g_\pi^2}{2}I_1(m_{\eta,V})\right)\Bigg] + [V\to A]\Bigg\}. \end{aligned} \tag{A32}$$

Similarly, the SU(2) chiral log terms in $B\to K$ are:

$$D_{\rm SU(2)}^{B\to K} = 0, \tag{A33}$$

$$\begin{aligned} {\rm logs}_{\perp,{\rm SU(2)}}^{B\to K} = \frac{1}{(4\pi f)^2}\Bigg\{ & \frac{1}{16}\sum_\Xi \left[-3g_\pi^2 I_1(m_{\pi,\Xi})\right] + \frac{3g_\pi^2}{4}I_1(m_{\pi,I}) \\ & + \frac{3g_\pi^2}{2}\left[2I_1(m_{\pi,V}) - 2I_1(m_{\eta,V})\right] + [V\to A]\Bigg\}. \end{aligned} \tag{A34}$$

Equations (A31), (A32), and (A34) are written with a structure similar to their SU(3) counterparts, which makes it easier to implement a unified computer code for the various choices of χPT studied in this paper.

3. Form factors in hard pion/kaon ChPT

The hard kaon (pion) continuum HMχPT for $B \to K$ and $B \to \pi$ semileptonic decays were derived in Refs. [107, 108]. The pion or kaon with large E is integrated out from the theory and its effects are absorbed into the LECs. We derive the hard kaon (pion) limit of the HMrSχPT in this section. We first study the asymptotic behavior of the integrals which contain E_π or E_K. We find that

$$I_2(m, E) \to A_0 E^2 \ln(E^2) + A_1 E^2 + A_2 \ln E - m^2 \ln(\frac{m^2}{\Lambda^2}) \ , \tag{A35}$$

$$J_1^{\rm sub}(m, E) \to B_0 E^2 \ln(E^2) + B_1 E^2 + B_2 \ln E + B_3 \ , \tag{A36}$$

in the large E limit, where the coefficients A_i and B_i are either constants or analytic functions of m. The divergent terms in the large E limit decouple from the expression. The analytic terms in m are absorbed into the redefinition of the LECs. So the rules to derive the hard kaon (pion) HMrSχPT are

- Replace the term $I_2(m, E)$ by $-I_1(m)$
- Remove $J_1^{\rm sub}(m, E)$ term

To compare our results with Refs. [107, 108], we set all taste splitting parameters, hairpin parameters and lattice spacings to zero. We then can reproduce the continuum hard kaon (pion) HMχPT results.

$$\log s_{\perp,{\rm SU}(3)}^{B\to\pi} = -(\frac{3}{4} + \frac{9}{4}g_\pi^2)\frac{I_1(m_\pi)}{(4\pi f)^2} - (\frac{1}{2} + \frac{3}{2}g_\pi^2)\frac{I_1(m_K)}{(4\pi f)^2} - (\frac{1}{12} + \frac{1}{4}g_\pi^2)\frac{I_1(m_\eta)}{(4\pi f)^2} \ , \tag{A37}$$

$$\log s_{\perp,{\rm SU}(3)}^{B\to K} = -(\frac{9}{4}g_\pi^2)\frac{I_1(m_\pi)}{(4\pi f)^2} - (1 + \frac{3}{2}g_\pi^2)\frac{I_1(m_K)}{(4\pi f)^2} - (\frac{1}{3} + \frac{1}{4}g_\pi^2)\frac{I_1(m_\eta)}{(4\pi f)^2} \ , \tag{A38}$$

$$D = 0 \ . \tag{A39}$$

Our derivation shows that $\log s_{\perp{\rm SU}(3)}^{B\to\pi} = \log s_{\parallel{\rm SU}(3)}^{B\to\pi}$ and $\log s_{\perp{\rm SU}(3)}^{B\to K} = \log s_{\parallel{\rm SU}(3)}^{B\to K}$ in the continuum, which is also found in Refs. [107, 108].

---

[1] J. A. Bailey *et al.* (Fermilab Lattice and MILC Collaborations), Phys. Rev. **D79**, 054507 (2009), arXiv:0811.3640 [hep-lat].

[2] J. A. Bailey *et al.* (Fermilab Lattice and MILC Collaboration), (2015), arXiv:1503.07839 [hep-lat].

[3] C. Bernard *et al.* (Fermilab Lattice and MILC Collaborations), Phys. Rev. **D79**, 014506 (2009), arXiv:0808.2519 [hep-lat].

[4] J. A. Bailey *et al.* (Fermilab Lattice and MILC Collaborations), Phys. Rev. **D89**, 114504 (2014), arXiv:1403.0635 [hep-lat].

[5] J. A. Bailey *et al.* (Fermilab Lattice and MILC Collaborations), (2015), arXiv:1503.07237 [hep-lat].

[6] K. A. Olive *et al.* (Particle Data Group), Chin. Phys. **C38**, 090001 (2014).

[7] J. A. Bailey *et al.* (Fermilab Lattice, MILC), (2015), arXiv:1507.01618 [hep-ph].

[8] J. A. Bailey *et al.* (Fermilab Lattice and MILC Collaborations), Phys. Rev. **D85**, 114502 (2012), arXiv:1202.6346 [hep-lat].

[9] J. A. Bailey *et al.* (Fermilab Lattice and MILC Collaborations), Phys. Rev. Lett. **109**, 071802 (2012), arXiv:1206.4992 [hep-ph].

[10] T. Hurth and M. Nakao, Annu. Rev. Nucl. Part. Sci. **60**, 645 (2010), arXiv:1005.1224 [hep-ph].

[11] M. Antonelli *et al.*, Phys. Rept. **494**, 197 (2010), arXiv:0907.5386 [hep-ph].

[12] B. Aubert *et al.* (BaBar Collaboration), Phys. Rev. Lett. **102**, 091803 (2009), arXiv:0807.4119 [hep-ex].

[13] J.-T. Wei *et al.* (Belle Collaboration), Phys. Rev. Lett. **103**, 171801 (2009), arXiv:0904.0770 [hep-ex].

[14] T. Aaltonen *et al.* (CDF Collaboration), Phys. Rev. Lett. **106**, 161801 (2011), arXiv:1101.1028 [hep-ex].

[15] T. Aaltonen *et al.* (CDF Collaboration), Phys. Rev. Lett. **107**, 201802 (2011), arXiv:1107.3753 [hep-ex].

[16] J. P. Lees *et al.* (BaBar Collaboration), Phys. Rev. **D86**, 032012 (2012), arXiv:1204.3933 [hep-ex].

[17] R. Aaij *et al.* (LHCb Collaboration), JHEP **1207**, 133 (2012), arXiv:1205.3422 [hep-ex].

[18] R. Aaij *et al.* (LHCb Collaboration), JHEP **1302**, 105 (2013), arXiv:1209.4284 [hep-ex].

[19] R. Aaij *et al.* (LHCb collaboration), JHEP **1406**, 133 (2014), arXiv:1403.8044 [hep-ex].

[20] J. L. Hewett, H. Weerts, *et al.*, *Fundamental Physics at the Intensity Frontier* (U.S. Department of Energy, 2012) arXiv:1205.2671 [hep-ex].

[21] C. Bouchard, G. P. Lepage, C. Monahan, H. Na, and J. Shigemitsu (HPQCD Collaboration), Phys. Rev. **D88**, 054509 (2013), arXiv:1306.2384 [hep-lat].

[22] C. Bouchard, G. P. Lepage, C. Monahan, H. Na, and J. Shigemitsu (HPQCD Collaboration), Phys. Rev. Lett. **111**, 162002 (2013), arXiv:1306.0434 [hep-ph].

[23] R. R. Horgan, Z. Liu, S. Meinel, and M. Wingate, Phys. Rev. **D89**, 094501 (2014), arXiv:1310.3722 [hep-lat].

[24] B. Grinstein, M. J. Savage, and M. B. Wise, Nucl. Phys. **B319**, 271 (1989).

[25] A. J. Buras, M. Misiak, M. Münz, and S. Pokorski, Nucl. Phys. **B424**, 374 (1994), arXiv:hep-ph/9311345 [hep-ph].

[26] C. Bobeth, M. Misiak, and J. Urban, Nucl. Phys. **B574**, 291 (2000), arXiv:hep-ph/9910220 [hep-ph].

[27] W. Altmannshofer *et al.*, JHEP **0901**, 019 (2009), arXiv:0811.1214 [hep-ph].

[28] B. Sheikholeslami and R. Wohlert, Nucl. Phys. **B259**, 572 (1985).

[29] A. X. El-Khadra, A. S. Kronfeld, and P. B. Mackenzie, Phys. Rev. **D55**, 3933 (1997), hep-lat/9604004.

[30] G. P. Lepage, L. Magnea, C. Nakhleh, U. Magnea, and K. Hornbostel, Phys. Rev. **D46**, 4052 (1992), arXiv:hep-lat/9205007 [hep-lat].

[31] C. G. Boyd, B. Grinstein, and R. F. Lebed, Phys. Rev. Lett. **74**, 4603 (1995), hep-ph/9412324.

[32] M. C. Arnesen, B. Grinstein, I. Z. Rothstein, and I. W. Stewart, Phys. Rev. Lett. **95**, 071802 (2005), hep-ph/0504209.

[33] C. Bourrely, I. Caprini, and L. Lellouch, Phys. Rev. **D79**, 013008 (2009), arXiv:0807.2722 [hep-ph].

[34] A. Bharucha, T. Feldmann, and M. Wick, JHEP **1009**, 090 (2010), arXiv:1004.3249 [hep-ph].

[35] R. Zhou *et al.* (Fermilab Lattice and MILC Collaborations), PoS **Lattice2011**, 298 (2011), arXiv:1111.0981 [hep-lat].

[36] R. Zhou *et al.* (Fermilab Lattice and MILC Collaborations), PoS **Lattice2012**, 120 (2012), arXiv:1211.1390 [hep-lat].

[37] R. Zhou (2013) arXiv:1301.0666 [hep-lat].

[38] D. Bečirević, N. Košnik, F. Mescia, and E. Schneider, Phys. Rev. **D86**, 034034 (2012), arXiv:1205.5811 [hep-ph].

[39] A. Ali, A. Y. Parkhomenko, and A. V. Rusov, Phys. Rev. **D89**, 094021 (2014), arXiv:1312.2523 [hep-ph].

[40] A. Bazavov *et al.*, Rev. Mod. Phys. **82**, 1349 (2010), arXiv:0903.3598 [hep-lat].

[41] MILC Collaboration, "asqtad.en06a," 10.15484/milc.asqtad.en06a/1178158 (2015).

[42] MILC Collaboration, "asqtad.en06b," 10.15484/milc.asqtad.en06b/1178159 (2015).

[43] MILC Collaboration, "asqtad.en05a," 10.15484/milc.asqtad.en05a/1178156 (2015).

[44] MILC Collaboration, "asqtad.en04a," 10.15484/milc.asqtad.en04a/1178155 (2015).

[45] MILC Collaboration, "asqtad.en15a," 10.15484/milc.asqtad.en15a/1178095 (2015).

[46] MILC Collaboration, "asqtad.en15b," 10.15484/milc.asqtad.en15b/1178096 (2015).

[47] MILC Collaboration, "asqtad.en15c," 10.15484/milc.asqtad.en15c/1178097 (2015).

[48] MILC Collaboration, "asqtad.en14a," 10.15484/milc.asqtad.en14a/1178094 (2015).

[49] MILC Collaboration, "asqtad.en13a," 10.15484/milc.asqtad.en13a/1178092 (2015).

[50] MILC Collaboration, "asqtad.en13b," 10.15484/milc.asqtad.en13b/1178093 (2015).

[51] MILC Collaboration, "asqtad.en12a," 10.15484/milc.asqtad.en12a/1178091 (2015).

[52] MILC Collaboration, "asqtad.en20a," 10.15484/milc.asqtad.en20a/1178036 (2015).

[53] MILC Collaboration, "asqtad.en20b," 10.15484/milc.asqtad.en20b/1178037 (2015).

[54] MILC Collaboration, "asqtad.en18a," 10.15484/milc.asqtad.en18a/1178033 (2015).

[55] MILC Collaboration, "asqtad.en18b," 10.15484/milc.asqtad.en18b/1178034 (2015).

[56] MILC Collaboration, "asqtad.en24a," 10.15484/milc.asqtad.en24a/1177873 (2015).

[57] C. W. Bernard *et al.*, Phys. Rev. **D64**, 054506 (2001), hep-lat/0104002.

[58] C. Aubin *et al.*, Phys. Rev. **D70**, 094505 (2004), arXiv:hep-lat/0402030 [hep-lat].

[59] M. Lüscher and P. Weisz, Commun. Math. Phys. **97**, 59 (1985).

[60] M. Lüscher and P. Weisz, Phys. Lett. **B158**, 250 (1985).

[61] Z. Hao, G. M. von Hippel, R. R. Horgan, Q. J. Mason, and H. D. Trottier, Phys. Rev. **D76**, 034507 (2007), arXiv:0705.4660 [hep-lat].

[62] T. Blum *et al.*, Phys. Rev. **D55**, 1133 (1997), hep-lat/9609036.

[63] G. P. Lepage, Nucl. Phys. Proc. Suppl. **60A**, 267 (1998), hep-lat/9707026.

[64] J. F. Lagaë and D. K. Sinclair, Phys. Rev. **D59**, 014511 (1999), hep-lat/9806014.

[65] G. P. Lepage, Phys. Rev. **D59**, 074502 (1999), arXiv:hep-lat/9809157.

[66] K. Orginos and D. Toussaint (MILC Collaboration), Phys. Rev. **D59**, 014501 (1999), hep-lat/9805009.

[67] K. Orginos, D. Toussaint, and R. L. Sugar (MILC Collaboration), Phys. Rev. **D60**, 054503 (1999), hep-lat/9903032.

[68] C. W. Bernard *et al.* (MILC Collaboration), Phys. Rev. **D61**, 111502 (2000), hep-lat/9912018.

[69] Y. Shamir, Phys. Rev. **D71**, 034509 (2005), hep-lat/0412014.

[70] Y. Shamir, Phys. Rev. **D75**, 054503 (2007), hep-lat/0607007.

[71] W.-J. Lee and S. R. Sharpe, Phys. Rev. **D60**, 114503 (1999), hep-lat/9905023.

[72] C. Bernard, Phys. Rev. **D73**, 114503 (2006), hep-lat/0603011.

[73] C. Bernard, M. Golterman, and Y. Shamir, Phys. Rev. **D77**, 074505 (2008), arXiv:0712.2560 [hep-lat].

[74] S. Prelovšek, Phys. Rev. **D73**, 014506 (2006), hep-lat/0510080.

[75] C. Bernard, C. E. DeTar, Z. Fu, and S. Prelovšek, Phys. Rev. **D76**, 094504 (2007), arXiv:0707.2402 [hep-lat].

[76] C. Aubin, J. Laiho, and R. S. Van de Water, Phys. Rev. **D77**, 114501 (2008), arXiv:0803.0129 [hep-lat].

[77] S. R. Sharpe and R. S. Van de Water, Phys. Rev. **D71**, 114505 (2005), hep-lat/0409018.

[78] S. Dürr, PoS **LAT2005**, 021 (2006), hep-lat/0509026.

[79] S. R. Sharpe, PoS **LAT2006**, 022 (2006), hep-lat/0610094.

[80] A. S. Kronfeld, PoS **LAT2007**, 016 (2007), arXiv:0711.0699 [hep-lat].

[81] G. C. Donald, C. T. H. Davies, E. Follana, and A. S. Kronfeld (HPQCD and Fermilab Lattice Collaborations), Phys. Rev. **D84**, 054504 (2011), arXiv:1106.2412 [hep-lat].

[82] A. S. Kronfeld, Phys. Rev. **D62**, 014505 (2000), hep-lat/0002008.

[83] M. B. Oktay and A. S. Kronfeld, Phys. Rev. **D78**, 014504 (2008), arXiv:0803.0523 [hep-lat].

[84] J. Harada, S. Hashimoto, K.-I. Ishikawa, A. S. Kronfeld, T. Onogi, and N. Yamada, Phys. Rev. **D65**, 094513 (2002), hep-lat/0112044.

[85] J. Harada, S. Hashimoto, A. S. Kronfeld, and T. Onogi, Phys. Rev. **D65**, 094514 (2002), arXiv:hep-lat/0112045 [hep-lat].

[86] J. A. Bailey, Y.-C. Jang, W. Lee, and J. Leem (SWME Collaboration), PoS **LATTICE2014**, 389 (2014), arXiv:1411.4227 [hep-lat].

[87] R. Sommer, Nucl. Phys. **B411**, 839 (1994), hep-lat/9310022.

[88] C. W. Bernard *et al.*, Phys. Rev. **D62**, 034503 (2000), hep-lat/0002028.

[89] A. Bazavov *et al.* (Fermilab Lattice and MILC Collaborations), Phys. Rev. **D85**, 114506 (2012), arXiv:1112.3051 [hep-lat].

[90] R. Arthur *et al.* (RBC, UKQCD), Phys.Rev. **D87**, 094514 (2013), arXiv:1208.4412 [hep-lat].

[91] M. Wingate, J. Shigemitsu, C. T. H. Davies, G. P. Lepage, and H. D. Trottier, Phys. Rev. **D67**, 054505 (2003), hep-lat/0211014.

[92] A. X. El-Khadra, A. S. Kronfeld, P. B. Mackenzie, S. M. Ryan, and J. N. Simone, Phys. Rev. **D64**, 014502 (2001), hep-ph/0101023.

[93] S.-W. Qiu *et al.* (Fermilab Lattice and MILC Collaborations), PoS **LATTICE2011**, 289 (2011), arXiv:1111.0677 [hep-lat].

[94] A. X. El-Khadra, E. Gámiz, A. S. Kronfeld, and M. A. Nobes, PoS **LAT2007**, 242 (2007), arXiv:0710.1437 [hep-lat].

[95] G. P. Lepage and P. B. Mackenzie, Phys. Rev. **D48**, 2250 (1993), arXiv:hep-lat/9209022 [hep-lat].

[96] Q. Mason *et al.* (HPQCD Collaboration), Phys. Rev. Lett. **95**, 052002 (2005), hep-lat/0503005.

[97] A. X. El-Khadra, E. Gámiz, and A. S. Kronfeld, in preparation.

[98] S. J. Brodsky, G. P. Lepage, and P. B. Mackenzie, Phys. Rev. **D28**, 228 (1983).

[99] J. L. Richardson, Phys. Lett. **B82**, 272 (1979).

[100] D. P. Menscher, *Charmonium and Charmed Mesons with Improved Lattice QCD*, Ph.D. thesis, University of Illinois (2005).

[101] C. Bernard *et al.* (Fermilab Lattice and MILC Collaborations), Phys. Rev. **D83**, 034503 (2011), arXiv:1003.1937 [hep-lat].

[102] E. T. Neil *et al.* (Fermilab Lattice and MILC Collaborations), PoS **LATTICE2011**, 320 (2011), arXiv:1112.3978 [hep-lat].

[103] G. P. Lepage *et al.*, Nucl. Phys. Proc. Suppl. **106**, 12 (2002), hep-lat/0110175.

[104] C. Morningstar, Nucl. Phys. Proc. Suppl. **109A**, 185 (2002), hep-lat/0112023.

[105] C. Aubin and C. Bernard, Phys. Rev. **D73**, 014515 (2006), arXiv:hep-lat/0510088 [hep-lat].

[106] C. Aubin and C. Bernard, Phys. Rev. **D76**, 014002 (2007), arXiv:0704.0795 [hep-lat].

[107] J. Bijnens and I. Jemos, Nucl. Phys. **B840**, 54 (2010), arXiv:1006.1197 [hep-ph].

[108] J. Bijnens and I. Jemos, Nucl. Phys. **B846**, 145 (2011), arXiv:1011.6531 [hep-ph].

[109] G. Colangelo, M. Procura, L. Rothen, R. Stucki, and J. Tarrus Castella, JHEP **1209**, 081 (2012), arXiv:1208.0498 [hep-ph].

[110] W. A. Bardeen, E. J. Eichten, and C. T. Hill, Phys. Rev. **D68**, 054024 (2003), hep-ph/0305049.

[111] A. M. Green, J. Koponen, C. McNeile, C. Michael, and G. Thompson (UKQCD Collaboration), Phys. Rev. **D69**, 094505 (2004), hep-lat/0312007.

[112] C. B. Lang, D. Mohler, S. Prelovsek, and R. M. Woloshyn, (2015), arXiv:1501.01646 [hep-lat].

[113] W. Detmold, C.-J. D. Lin, and S. Meinel, Phys. Rev. Lett. **108**, 172003 (2012), arXiv:1109.2480 [hep-lat].

[114] W. Detmold, C.-J. D. Lin, and S. Meinel, Phys. Rev. **D85**, 114508 (2012), arXiv:1203.3378 [hep-lat].

[115] J. Flynn *et al.* (RBC/UKQCD), (2015), arXiv:1506.06413 [hep-lat].

[116] J. M. Flynn *et al.* (RBC and UKQCD Collaborations), PoS **LATTICE2013**, 408 (2014), arXiv:1311.2251 [hep-lat].

[117] F. Bernardoni, J. Bulava, M. Donnellan, and R. Sommer (ALPHA Collaboration), Phys. Lett. **B740**, 278 (2015), arXiv:1404.6951 [hep-lat].

[118] D. Bečirević, S. Fajfer, and J. F. Kamenik, PoS **LAT2007**, 063 (2007), arXiv:0710.3496 [hep-lat].

[119] D. Arndt and C. J. D. Lin, Phys. Rev. **D70**, 014503 (2004), hep-lat/0403012.

[120] Y. Amhis *et al.* (Heavy Flavor Averaging Group), (2012), arXiv:1207.1158 [hep-ex].

[121] S. Aoki *et al.* (Flavour Lattice Averaging Group), Eur. Phys. J. **C74**, 2890 (2014), arXiv:1310.8555 [hep-lat].

[122] T. Becher and R. J. Hill, Phys. Lett. **B633**, 61 (2006), hep-ph/0509090.

[123] C. Bobeth, G. Hiller, D. van Dyk, and C. Wacker, JHEP **1201**, 107 (2012), arXiv:1111.2558 [hep-ph].

[124] B. Grinstein and D. Pirjol, Phys. Rev. **D70**, 114005 (2004), arXiv:hep-ph/0404250 [hep-ph].

[125] T. Becher, R. J. Hill, and M. Neubert, Phys. Rev. **D72**, 094017 (2005), arXiv:hep-ph/0503263 [hep-ph].

[126] A. Ali, B. D. Pecjak, and C. Greub, Eur. Phys. J. **C55**, 577 (2008), arXiv:0709.4422 [hep-ph].

[127] C. Bobeth, G. Hiller, and D. van Dyk, JHEP **1007**, 098 (2010), arXiv:1006.5013 [hep-ph].

[128] M. Beylich, G. Buchalla, and T. Feldmann, Eur. Phys. J. **C71**, 1635 (2011), arXiv:1101.5118 [hep-ph].

[129] W.-S. Hou, M. Kohda, and F. Xu, Phys. Rev. **D90**, 013002 (2014), arXiv:1403.7410 [hep-ph].

[130] G. Burdman, Z. Ligeti, M. Neubert, and Y. Nir, Phys. Rev. **D49**, 2331 (1994), arXiv:hep-ph/9309272 [hep-ph].

[131] M. B. Wise, Phys. Rev. **D45**, 2188 (1992).

[132] J. L. Hewett and D. G. Hitlin, eds., *The Discovery potential of a Super B Factory* (SLAC, Menlo Park, 2005) arXiv:hep-ph/0503261 [hep-ph].

[133] N. Isgur and M. B. Wise, Phys. Rev. **D42**, 2388 (1990).

[134] B. Colquhoun *et al.* (HPQCD), (2015), arXiv:1503.05762 [hep-lat].

[135] J. Charles, A. Le Yaouanc, L. Oliver, O. Pene, and J. C. Raynal, Phys. Rev. **D60**, 014001 (1999), arXiv:hep-ph/9812358 [hep-ph].

[136] M. Beneke and T. Feldmann, Nucl. Phys. **B592**, 3 (2001), arXiv:hep-ph/0008255 [hep-ph].

[137] P. Ball and R. Zwicky, JHEP **0604**, 046 (2006), arXiv:hep-ph/0603232 [hep-ph].

[138] V. M. Braun, D. Y. Ivanov, and G. P. Korchemsky, Phys. Rev. **D69**, 034014 (2004), arXiv:hep-ph/0309330 [hep-ph].

[139] A. Khodjamirian, T. Mannel, and N. Offen, Phys. Lett. **B620**, 52 (2005), arXiv:hep-ph/0504091 [hep-ph].

[140] S. J. Lee and M. Neubert, Phys. Rev. **D72**, 094028 (2005), arXiv:hep-ph/0509350 [hep-ph].

[141] R. Arthur *et al.* (RBC and UKQCD), Phys. Rev. **D83**, 074505 (2011), arXiv:1011.5906 [hep-lat].

[142] K. Chetyrkin, J. H. Kuhn, and M. Steinhauser, Comput.Phys.Commun. **133**, 43 (2000), arXiv:hep-ph/0004189 [hep-ph].

[143] G. Bell, M. Beneke, T. Huber, and X.-Q. Li, Nucl. Phys. **B843**, 143 (2011), arXiv:1007.3758 [hep-ph].

[144] A. Khodjamirian, T. Mannel, A. A. Pivovarov, and Y.-M. Wang, JHEP **1009**, 089 (2010), arXiv:1006.4945 [hep-ph].

[145] S. L. Glashow, D. Guadagnoli, and K. Lane, Phys. Rev. Lett. **114**, 091801 (2015), arXiv:1411.0565 [hep-ph].

[146] D. Du, A. X. El-Khadra, S. Gottlieb, A. S. Kronfeld, J. Laiho, E. Lunghi, R. S. Van de Water, and R. Zhou, (2015), arXiv:1510.02349 [hep-ph].

[147] A. Bazavov *et al.* (MILC Collaboration), Phys. Rev. **D82**, 074501 (2010), arXiv:1004.0342 [hep-lat].

[148] A. Bazavov *et al.* (MILC Collaboration), Phys. Rev. **D87**, 054505 (2013), arXiv:1212.4768 [hep-lat].

[149] E. Follana *et al.* (HPQCD Collaboration), Phys. Rev. **D75**, 054502 (2007), arXiv:hep-lat/0610092 [hep-lat].

[150] A. Bazavov *et al.* (Fermilab Lattice and MILC Collaborations), Phys. Rev. Lett. **112**, 112001 (2014), arXiv:1312.1228 [hep-ph].

[151] A. Bazavov *et al.* (Fermilab Lattice and MILC Collaborations), Phys. Rev. **D90**, 074509 (2014), arXiv:1407.3772 [hep-lat].

[152] D. Bečirević, S. Prelovšek, and J. Zupan, Phys. Rev. **D67**, 054010 (2003), hep-lat/0210048.

[153] D. Bečirević, S. Prelovšek, and J. Zupan, Phys. Rev. **D68**, 074003 (2003), hep-lat/0305001.

[154] D. Bečirević, S. Fajfer, and J. F. Kamenik, JHEP **06**, 003 (2007), hep-ph/0612224.

[155] S. Di Vita *et al.*, PoS **LAT2010** (2011), arXiv:1104.0869 [hep-lat].

[156] C. Aubin and C. Bernard, Phys. Rev. **D68**, 034014 (2003).